iScience

CellPress

Article

A Non-canonical Function of BMAL1 Metabolically Limits Obesity-Promoted Triple-Negative Breast Cancer

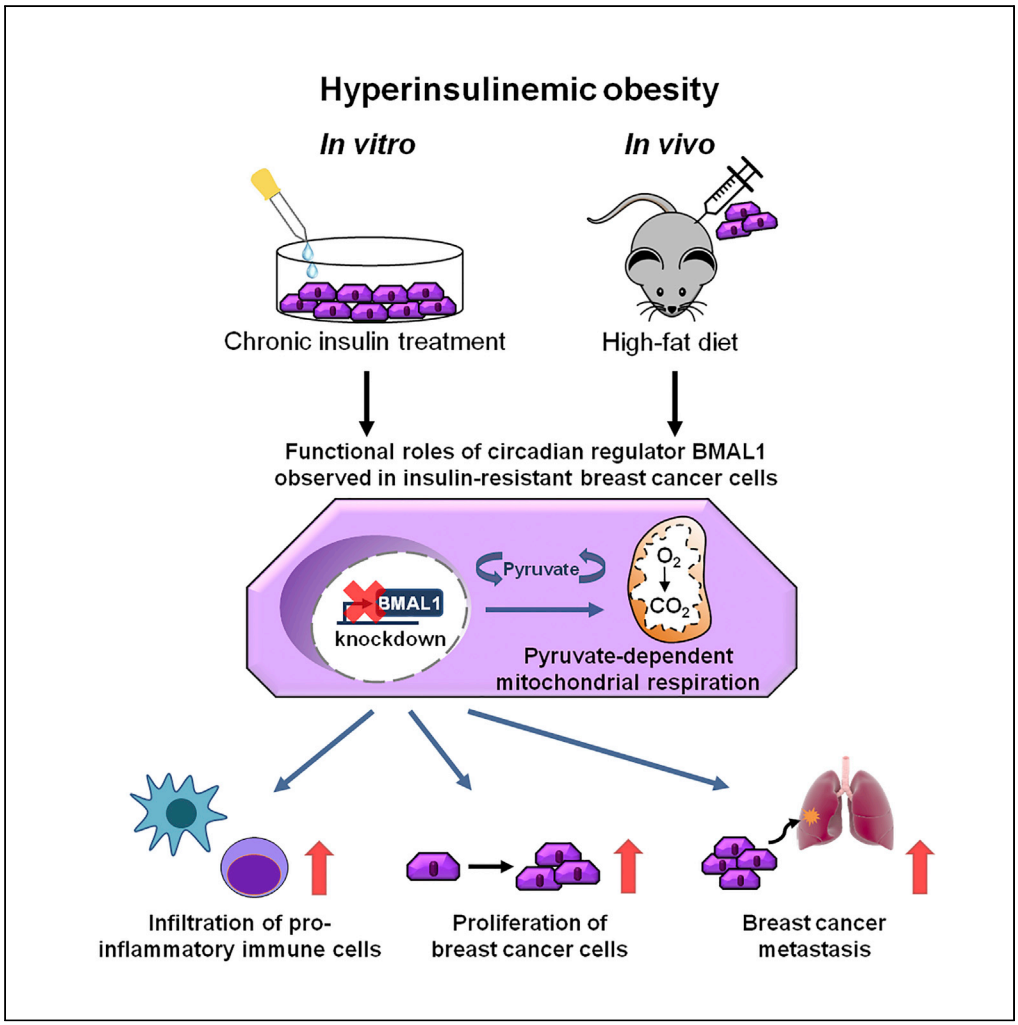

Cassandra A. Ramos, Ching Ouyang, Yue Qi, ..., Mark A. LaBarge, Victoria L. Seewaldt, David K. Ann

dann@coh.org

HIGHLIGHTS

Circadian regulator BMAL1 rewires metabolism in a chronic insulin-treated TNBC model

Pyruvate links BMAL1 to mitochondrial bioenergetics

BMAL1 suppresses tumor proliferation and metastasis in hyperinsulinemic obese mice

BMAL1 influences tumor microenvironment in high-fat-diet-fed mice

Ramos et al., iScience *23*, 100839
February 21, 2020 © 2020 The Authors.
https://doi.org/10.1016/j.isci.2020.100839

iScience

CellPress

Article

A Non-canonical Function of BMAL1 Metabolically Limits Obesity-Promoted Triple-Negative Breast Cancer

Cassandra A. Ramos,[1,2] Ching Ouyang,[3,4] Yue Qi,[1] Yiyin Chung,[1] Chun-Ting Cheng,[1] Mark A. LaBarge,[2,5] Victoria L. Seewaldt,[2,5] and David K. Ann[1,2,6,*]

SUMMARY

The epidemiological association between disrupted circadian rhythms and metabolic diseases is implicated in increased risk of human breast cancer and poor therapeutic outcomes. To define a metabolic phenotype and the underlying molecular mechanism, we applied chronic insulin treatment (CIT) to an *in vitro* model of triple-negative breast cancer to directly address how BMAL1, a key circadian transcription factor, regulates cancer cell respiration and governs tumor progression. At the cellular level, BMAL1 suppresses the flexibility of mitochondrial substrate usage and the pyruvate-dependent mitochondrial respiration induced by CIT. We established an animal model of diet-induced obesity/hyperinsulinemia and observed that BMAL1 functions as a tumor suppressor in obese, but not lean, mice. Downregulation of BMAL1 is associated with higher risk of metastasis in human breast tumors. In summary, loss of BMAL1 in tumors confers advantages to cancer cells in both intrinsic mitochondrial metabolism and extrinsic inflammatory tumor microenvironment during pre-diabetic obesity/hyperinsulinemia.

INTRODUCTION

Rhythmic oscillations in cellular activity are coordinated by genes that comprise the core circadian machinery (Bell-Pedersen et al., 2005). The notion that circadian rhythm disruptions lead to an increased likelihood of mammary tumor development is supported by studies that female workers taking frequent night shifts have disrupted internal clocks and an increased risk of developing breast cancer (BC) (Davis et al., 2001; Schernhammer et al., 2001; Wegrzyn et al., 2017). It has been reported that circadian genes have anti-tumor roles in multiple cancer types (de Assis et al., 2018; Papagiannakopoulos et al., 2016; Tang et al., 2017) and may act as tumor suppressors by regulating a wide variety of pathophysiological events, including cellular metabolism and pathogenesis of cancer (Cederroth et al., 2019; Lesicka et al., 2018; Lin and Farkas, 2018). Indeed, disrupted circadian rhythm likely affects multiple hallmarks of cancer, including proliferative signaling maintenance, cell death resistance, replicative immortality, invasion and metastasis activation, and energy metabolism reconfiguration (Hanahan and Weinberg, 2011).

Epidemiological data also suggest that disrupted circadian rhythm is strongly associated with metabolic syndrome (Verlande and Masri, 2019). Multiple factors common to metabolic syndrome and its related disorders have been shown to promote BC tumor growth and progression (Hursting et al., 2012). For example, hyperinsulinemia, or elevated circulating insulin levels, is a hallmark of obesity and pre-diabetes and is associated with higher BC incidence and poor prognosis (Del Giudice et al., 1998; Goodwin et al., 2002; Gunter et al., 2009; Lawlor et al., 2004; Lipscombe et al., 2006; Tsujimoto et al., 2017). Moreover, multiple reports indicate that metabolic diseases differentially impact individual subtypes of BC (Capasso et al., 2014; Garcia-Estevez and Moreno-Bueno, 2019; Yang et al., 2011). Overall, despite current studies demonstrating a close relationship among circadian disruption, metabolic syndrome, and cancer progression, the mechanisms linking these together are not yet systematically established.

Circadian clocks are orchestrated by a gene network through transcriptional regulation (Partch et al., 2014). Circadian-controlled genes are transcribed after initiation by the transcription factor heterodimer complex comprising Brain and Muscle Arnt-Like (BMAL) and Circadian Locomotor Output Cycles Kaput (CLOCK) (Sahar and Sassone-Corsi, 2009). Together with BMAL1 (gene name: *ARNTL*) and CLOCK, the core circadian genes comprise the machinery that implements the oscillations in cellular activity (Bell-Pedersen

[1]Department of Diabetes Complications and Metabolism, Beckman Research Institute, City of Hope, Duarte, CA 91010, USA

[2]Irell & Manella Graduate School of Biological Sciences, City of Hope, Duarte, CA 91010, USA

[3]Center for Informatics, City of Hope National Medical Center, Duarte, CA 91010, USA

[4]Department of Computational and Quantitative Medicine, Beckman Research Institute, City of Hope, Duarte, CA 91010, USA

[5]Department of Population Sciences, Beckman Research Institute, City of Hope, Duarte, CA 91010, USA

[6]Lead Contact

*Correspondence: dann@coh.org

https://doi.org/10.1016/j.isci.2020.100839

This is an open access article under the CC BY-NC-ND license (http://creativecommons.org/licenses/by-nc-nd/4.0/).

et al., 2005). Therefore, BMAL1 is an essential clock gene affecting all rhythmic behaviors as the loss of BMAL1 ensures that the circadian heterodimer is disrupted (Bunger et al., 2000). A number of reports have documented the crosstalk between BMAL1 function and insulin signaling, mitochondrial function, and lipid metabolism in non-cancer tissues (Breit et al., 2018; Dang et al., 2016; Jacobi et al., 2015; Liu et al., 2016; Luciano et al., 2018; Luo et al., 2019; Marcheva et al., 2010; McGinnis et al., 2017; Zhang et al., 2014). In addition, BMAL1 transcriptionally activates genes important for its own feedback loop (Sato et al., 2006) as well as many cellular processes, including mitochondrial dynamics, cell cycle regulation, and stress responses (Hatanaka et al., 2010; Jacobi et al., 2015; Rey et al., 2011). Global and liver-specific knockout of BMAL1 resulted in hyperlipidemia and increased lipoprotein production (Pan et al., 2016). However, the functional role of BMAL1 in BC cell metabolism and tumor progression remains largely unknown.

Understanding how circadian disruption and metabolic dysregulation influence BC can help elucidate the underlying biological mechanisms, especially in the basal-like (BL)/triple-negative BC (TNBC) subtype for which there is currently no effective therapeutic target. In this study, we developed two independent cell models, *in vitro* and *in vivo*, to investigate how the deficiency of intrinsic BMAL1 affects cellular metabolic homeostasis and tumor progression of TNBC. We demonstrate a previously unrecognized effect by tumor-intrinsic BMAL1 on shaping the mitochondrial fuel flexibility and anti-tumor landscape. Our observations provide insights into the mechanism underlying BMAL1-mediated TNBC suppression and evidence that BMAL1 downregulation in combination with hyperinsulinemic obesity exacerbates TNBC progression and aggressiveness. We discuss the implications of using BMAL1 as a marker, along with diet management, for cancer prevention and therapeutics.

RESULTS

Developing an *In Vitro* Cell Model to Investigate BMAL1 Function in TNBC

Circadian rhythms not only vary among different organisms but also can be unique in different tissue organs within the same organism (Yoo et al., 2004). Investigation across cancers originated from different tissues suggested that altered expression of clock genes often shows cancer type-specific pattern and is associated with oncogenic pathways, clinical outcomes, and molecular subtypes (Ye et al., 2018). To examine the expression profile of canonical core circadian genes across different cancer types, we investigated The Cancer Genome Atlas (TCGA) Pan-Cancer datasets. Consistent with the corroborated link between circadian disruption and BC (Blakeman et al., 2016), the expression of *ARNTL*/BMAL1 was significantly down-regulated in primary tumor samples compared with normal tissues in multiple cancer types, including BC (Figure S1A). As BC is highly heterogeneous and can be classified into different molecular subtypes (Perou et al., 2000), subsequent analysis using unsupervised hierarchical clustering revealed that the BL subtype has a distinct circadian gene expression profile among the PAM50 molecular subtypes (Figure 1A). Most tumors of BL subtype do not express receptors for estrogen, progesterone, and HER2, the major characteristics of TNBC. This subtype is more aggressive and has a poorer prognosis than other BC subtypes (Subik et al., 2010; Toft and Cryns, 2011). The average expression of the core circadian genes (Figure 1B) and *ARNTL*/BMAL1 (Figure 1C) in the BL and HER2-enriched subtypes was significantly lower compared with the other subtypes. We thereby sought to further study BMAL1 deficiency with the focus on BL/TNBC because circadian rhythm disruption may affect BC in a subtype-dependent manner.

To identify a suitable *in vitro* cell model, we evaluated a panel of 51 BC cell lines. The gene expression profiles are in general agreement with our observations from the TCGA clinical samples, confirming that circadian gene expression levels differ among the BC subtypes. Among the BL/TNBC cell lines, MDA-MB-231 was selected for its low- to mid-range abundance of circadian gene expression (Figure S1B) and *ARNTL* message (Figure S1C). Next, to develop a metabolic phenotype, MDA-MB-231 cells were continuously passaged in media supplemented with insulin for more than 10 passages, referred to as chronic insulin treatment (CIT). To mimic the insulin levels in a post-meal, fed state during pre-diabetes (high insulin with normal glucose), CIT cells treated with 10 or 100 nM insulin were assayed to verify that these cells were no longer sensitive to additional insulin stimulation. As shown in Figure 1D, no strong increase in insulin signaling activation was observed in serum/insulin-deprived (24 h) CIT cells stimulated with a high concentration of insulin at 100 nM, indicating the development of insulin resistance. To examine the effect of CIT on circadian outputs, a serum shock procedure was applied to stimulate and synchronize oscillations of circadian genes (Balsalobre et al., 1998). Cells grown without insulin exhibited a standard *ARNTL* mRNA oscillation, whereas we observed decreased amplitude for short-term insulin treatment and an early peak

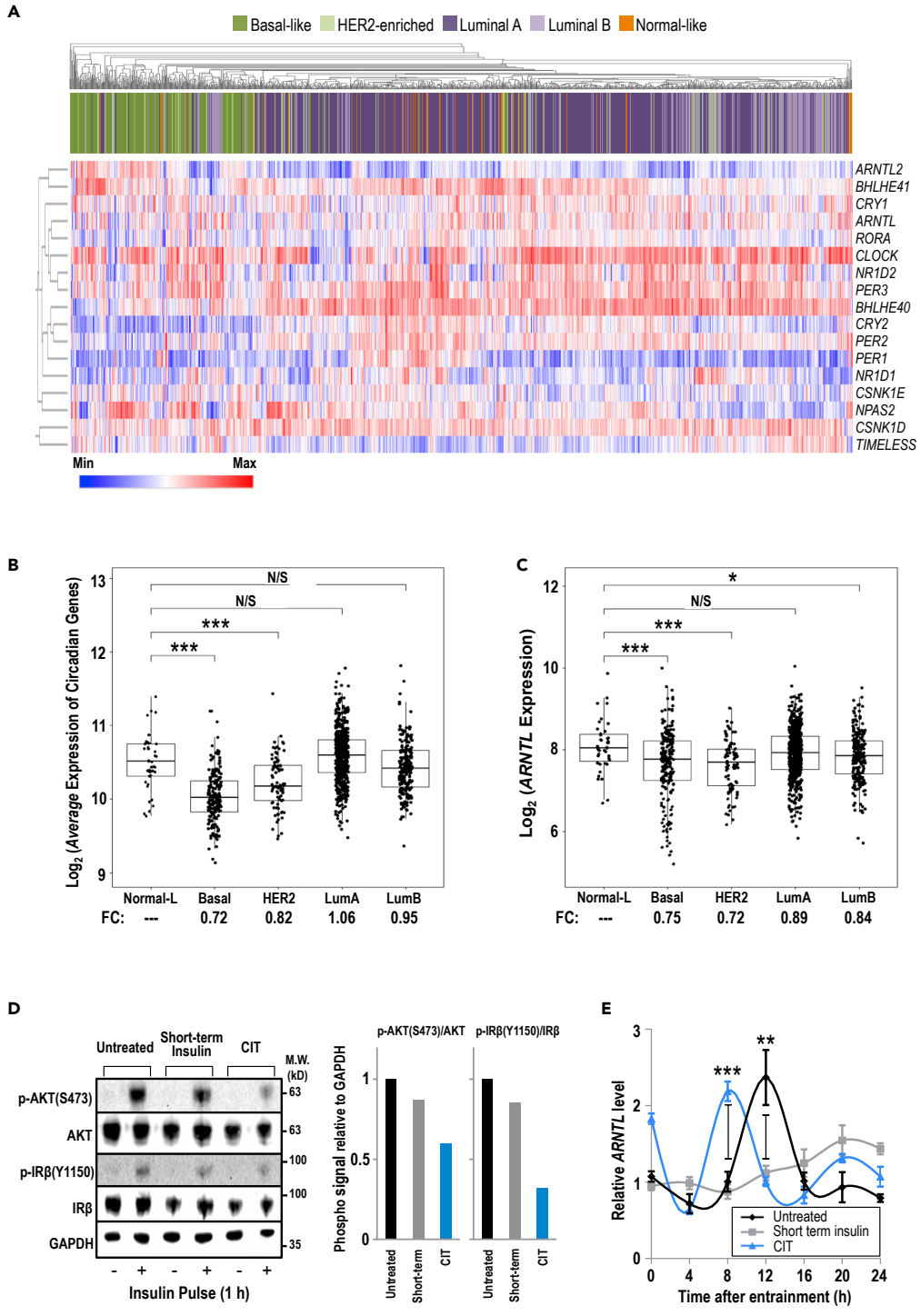

Figure 1. Expression of Core Circadian Genes Is Altered in BC

(A) The 1,097 BC patient samples from the TCGA database were analyzed via unsupervised hierarchical clustering to show circadian expression profiles among the PAM50 subtypes: Basal-like, HER2-enriched, Luminal A, Luminal B, and Normal-like.

(B and C) The patient samples were analyzed for average expression of circadian genes (B) and *ARNTL* expression (C), grouped by BC subtypes.

(D) Immunoblot analysis (left panel) of markers of active insulin signaling—phosphorylated AKT and phosphorylated IRβ—were examined to reflect relative levels of insulin signaling. GAPDH serves as a loading control. Quantification of

Figure 1. *Continued*
phosphorylated AKT/total AKT and phosphorylated IRβ/total IRβ is shown relative to GAPDH levels, and signal in untreated cells is set to 1 (*right panel*). CIT: chronic insulin treatment.
(E) Cells were entrained by serum shock. Total RNA was collected every 4 h and analyzed by qRT-PCR. Data are shown as mean ± SD; n = 3; one-way ANOVA with Tukey's post hoc test. The *GAPDH* mRNA level of untreated cells at 0 h is set to 1.
(B, C, and E) N/S $p > 0.05$; *$p > 0.05$; **$p < 0.05$; ***$p < 0.001$. See also Figures S1 and S2.

for CIT (Figure 1E). Of note, we also tested the same assay with additional cell lines having different abundance of endogenous BMAL1 (Figure S2A). Alteration of *ARNTL* mRNA oscillation was again observed in another TNBC cell line BT549 (Figure S2B), as well as progesterone receptor-positive MCF7 cells (Figure S2C), suggesting that the effect of short-term insulin and CIT on *ARNTL* mRNA oscillation is common. However, the alteration pattern may vary with different cell types.

The Interplay between BMAL1 and Mitochondrial Adaptations to CIT

The molecular interplay between circadian rhythms and cellular metabolism has been delineated as circadian genes control the nicotinamide adenine dinucleotide (NAD^+) salvage pathway (Nakahata et al., 2009). Thus, we conducted oscillating circadian-controlled NAD^+ assays (Ramsey et al., 2009) with untreated and CIT cells. CIT cells showed a faster peak time and a higher steady-state NAD^+/NADH ratio than those in insulin-responsive MDA-MB-231 cells (Figure S3A), demonstrating the links among insulin signaling, circadian output, and cellular metabolism. Also, the oxidation of NADH to NAD^+ links the tricarboxylic acid (TCA) cycle to ATP generation in mitochondria. Based on the above results, we tested the hypothesis that mitochondrial activity may partake in BMAL1 regulation. In ρ^0 cells (depleted of mitochondrial DNA), we observed a significant decrease in the steady-state BMAL1 protein levels (Figure S3B) and mRNA levels of *ARNTL*/BMAL1, along with its direct target *NAMPT*, irrespective of CIT (Figure S3C). Unlike in MDA-MB-231 cells (Figure 1E), there was no detectable difference in *ARNTL* message oscillation between untreated and CIT ρ^0 cells (Figure S3D). We concluded that the mitochondrial activity is indispensable for the expression and CIT-mediated regulation of BMAL1 and its downstream NAD^+-regulating target gene.

Next, we tested the state of mitochondrial respiration in the context of decreased BMAL1 expression. *ARNTL*-targeting small interfering RNA (siRNA) (siBMAL1) was designed and used to decrease BMAL1 abundance by nearly 90% (Figure 2A). In both untreated and CIT MDA-MB-231 cells, *ARNTL*knockdown produced higher levels of intracellular ATP (Figure 2B). Moreover, following CIT, BMAL1-knockdown cells produced a higher mitochondria-specific reactive oxygen species signal (reflecting electrons leaking from the electrochemical gradient) compared with control cells (Figure 2C). Together, these data suggested that BMAL1 regulates bioenergetic homeostasis and possibly other respiration outputs.

To pinpoint the involvement of BMAL1 in mitochondrial bioenergetics, oxygen consumption rate (OCR) was measured in untreated or CIT MDA-MB-231 cells. In control-knockdown cells, CIT increased OCR in a dose-dependent manner (Figure S3E), and an opposite OCR pattern was observed in BMAL1-knockdown cells (Figure S3F). BMAL1 knockdown increased basal respiration over control knockdown in untreated cells (Figure S3G, left panel). Also, BMAL1 was required for CIT to increase maximum respiration, a measurement of respiratory capacity, in a dose-dependent manner (Figure S3G, right panel). Given the fact that BMAL1 suppresses basal OCR in untreated cells and promotes maximal OCR in CIT cells, BMAL1 conceivably plays a key role in the mitochondrial metabolic adaptation to CIT.

We then investigated how BMAL1-mediated mitochondrial adaptations affect other metabolic parameters by measuring the levels of neutral lipid droplets, a nutrient source for cancer (Petan et al., 2018). Before assaying, MDA-MB-231 cells were starved of glucose to promote fatty acid mobilization (Rambold et al., 2015). We observed that BMAL1 knockdown increased the amounts of lipid droplets in both untreated and CIT cells (Figure S4A). Also, another functional consequence of CIT and BMAL1knockdown was an increase in the sensitivity to metformin (Figure S4B), a biguanide that causes oxidative stress by inhibiting mitochondrial complex I (Mayer et al., 2015). Last, by measuring extracellular acidification rate, we concluded that neither BMAL1 nor CIT impacted glycolytic activity (Figures S4C–S4E) in MDA-MB-231 cells.

Pyruvate Links BMAL1 to Mitochondrial Bioenergetics

Pyruvate is a key link between glycolysis and TCA cycle (Figure S5A). Based on the above-mentioned results, we hypothesized that BMAL1 serves a distinct role in regulating pyruvate utilization in untreated and CIT cells. To

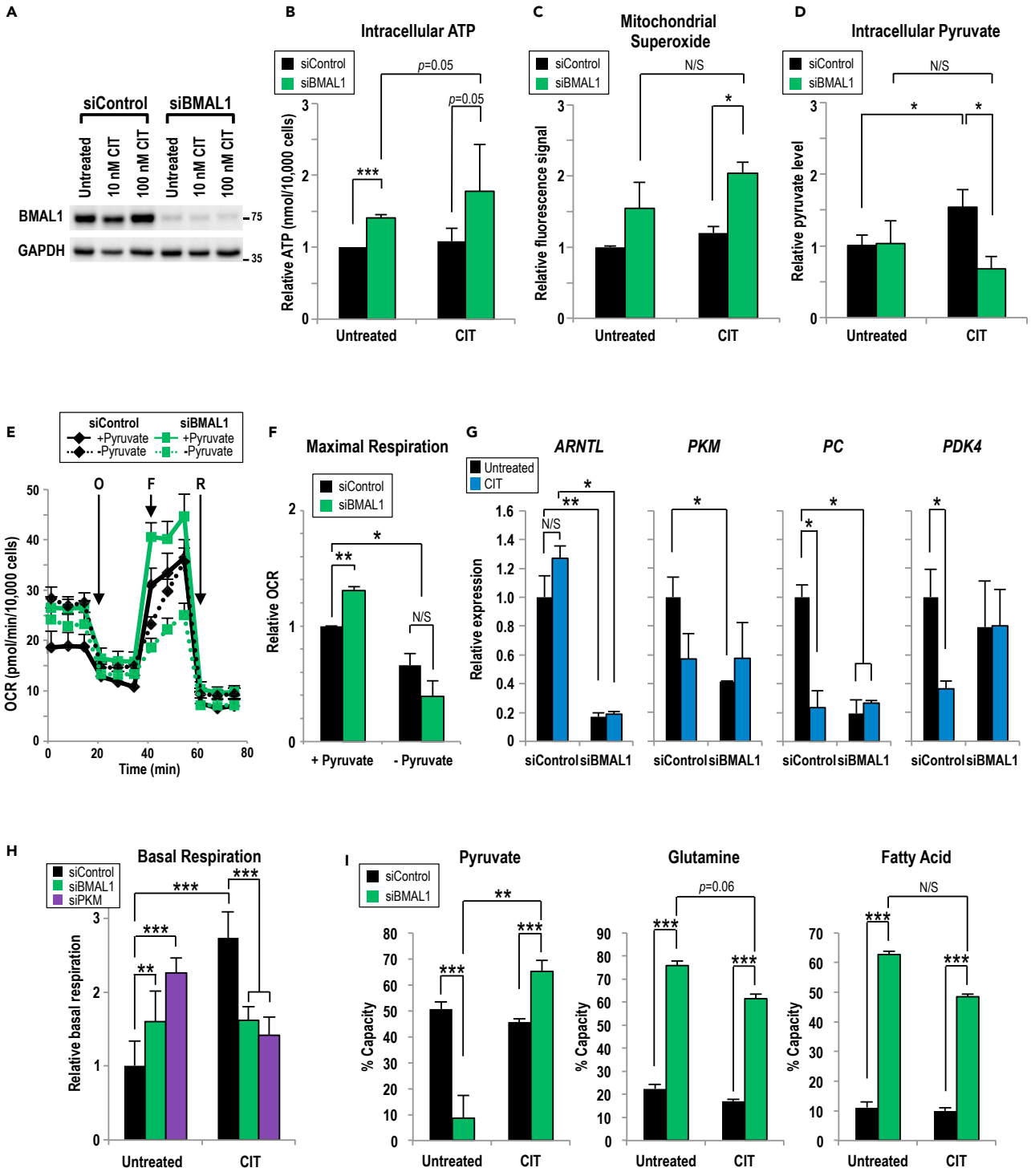

Figure 2. BMAL1 Mediates Pyruvate Utilization during Chronic Insulin Treatment

(A) Representative immunoblot showing the CIT effect on BMAL1 in MDA-MB-231 cells. BMAL1-targeting or control siRNA was transiently transfected into untreated or CIT cells. Owing to different levels of protein abundance, BMAL1 blot with longer exposure time, compared with GAPDH blot, is shown. (B and C) (B) Intracellular levels of ATP and (C) mitochondrial superoxide were assayed in MDA-MB-231 cells grown without insulin (Untreated) or over 10 passages of insulin (100 nM, CIT) and then transiently transfected with control or BMAL1-targeting siRNA. Measurements are normalized to cell number. n = 3; independent samples t test.

Figure 2. *Continued*

(D) Intracellular pyruvate was measured in MDA-MB-231 cells not treated or chronically treated with insulin (100 nM, CIT) and transfected with control or BMAL1-targeting siRNA. Pyruvate levels are normalized to cell number. n = 3.

(E) One representative oxygen consumption rate (OCR) profile of Mito Stress Test with MDA-MB-231 cells containing control or BMAL1-targeting siRNA in media ± pyruvate.

(F) Pyruvate is required for maximal respiration, calculated from (E). n ≥ 3.

(G) The relative levels of mRNA encoding pyruvate-regulating enzymes from untreated or CIT MDA-MB-231 cells transfected with control or BMAL1/*ARNTL*-targeting siRNA, quantified using qRT-PCR. n = 3.

(H) The basal respiration in untreated or CIT MDA-MB-231 cells transfected with control, BMAL1/*ARNTL*, or *PKM*-targeting siRNA were analyzed using Mito Stress Test. Measurements are normalized to cell number. n = 3; one-way ANOVA with Tukey's post hoc.

(I) The capacity to oxidize pyruvate (left panel), glutamine (middle panel), and fatty acids (right panel) in control or siBMAL1-transfected, untreated, or CIT MDA-MB-231 cells was analyzed using the Mito Fuel Flex Test. n = 3; one-way ANOVA with Tukey's post hoc.

(B–I) Data are shown as mean ± SD; *p < 0.05; **p < 0.01; ***p < 0.001. (B–D and F–I) one-way ANOVA with Tukey's post hoc. See also Figures S3–S6.

address this possibility in different BC cells, intracellular pyruvate levels were measured in MDA-MB-231, along with BT549 and MCF7 cells. As we observed in MDA-MB-231 cells (shown in Figure 2A), CIT did not affect steady-state level of BMAL1 in either BT549 or MCF7 cells (Figure S5B). However, CIT increased pyruvate levels in control (without BMAL1 knockdown) MDA-MB-231 (Figure 2D) and BT-549 (Figure S5C) cells compared with their untreated cells. Also, pyruvate level was not affected by BMAL1 knockdown in untreated MDA-MB-231 cells (Figure 2D). In contrast, BMAL1 knockdown in CIT cells decreased pyruvate levels in all three (MDA-MB231, BT549, and MCF7) cell lines (Figures 2D, S5C, and S5E), suggesting that BMAL1 suppresses pyruvate utilization during CIT adaptation. We then measured OCR in the presence and absence of external pyruvate in MDA-MB-231 cells (Figure 2E). As expected, the increased maximal respiration by BMAL1 knockdown depended on external pyruvate availability (Figure 2F).

Because BMAL1 is a transcription factor, we posited that BMAL1 regulates genes that metabolize pyruvate (Deng et al., 2018). We found that BMAL1 knockdown reduced the expression of pyruvate kinase (*PKM*) and pyruvate carboxylase (*PC*) (converting phosphoenolpyruvate to pyruvate and converting pyruvate to oxaloacetate, as shown in Figure S5A) in untreated MDA-MB-231 cells (Figure 2G). In comparison, BMAL1 knockdown also markedly decreased *PKM*, *PC*, and *PDK4* mRNA levels in CIT BT549 (Figure S5D), but only showed relatively minor effect in MCF7 cells (Figure S5F), suggesting a context-dependent role of BMAL1 in regulating pyruvate metabolism enzyme expression in different BC cells. To test if the effects of BMAL1 on OCR are mediated through its regulation of PKM abundance, we applied *PKM*-targeting siRNA to lower PKM expression in MDA-MB-231 cells and assayed for mitochondrial respiration activity. Consistently, PKM knockdown increased OCR in untreated cells, but decreased OCR in CIT MDA-MB-231 cells, mimicking the effects seen in BMAL1knockdown (Figure 2H). The decreased PC activity could also render pyruvate less available to mitochondria (Perry et al., 2015). Together, these findings underscored a specific role of BMAL1 in regulating pyruvate metabolism.

To corroborate that BMAL1 affects substrate utilization, specific inhibitors were used to block three major mitochondrial fuels: glutamine, long-chain fatty acids, and pyruvate. Mito Fuel Flex assays demonstrated that BMAL1 knockdown altered substrate capacity, or the ability of cells to increase oxidation of particular fuel to compensate for inhibition of alternative fuels. Specifically, BMAL1knockdown increased glutamine and fatty acid oxidation capacity in both untreated and CIT cells (Figure 2I, middle and right panels), indicating that BMAL1 suppresses glutamine and fatty acid utilization in MDA-MB-231 cells. However, BMAL1 knockdown increased the capacity of pyruvate oxidation under CIT, but decreased it in the insulin-sensitive cells (Figure 2I, left panel). Finally, compromised BMAL1 decreased pyruvate (Figure S6A), but not glutamine (Figure S6B) and fatty acid (Figure S6C), dependency in mitochondria of CIT cells. These results demonstrated that BMAL1 regulates substrate usage and that CIT cells require BMAL1 to suppress substrate flexibility. This is consistent with our observations that BMAL1 knockdown mediates reduction of message abundance of key pyruvate metabolism-regulating enzymes (Figure 2G). Altogether, we surmised that CIT and BMAL1 counterbalanced the regulation of mitochondrial activity. This observed dual regulation of pyruvate by both BMAL1 and insulin would explain how insulin context alters the effect by BMAL1 on tumor cell metabolism.

BMAL1 Suppresses HFD-Induced Tumor Growth *In Vivo*

To further establish whether BMAL1 regulates tumor progression *in vivo*, we used wild-type female C57BL/6 mice coupled with mouse mammary tumor E0771 cells orthotopically implanted in syngeneic lean and obese mice (Figure S7A). The advantage of using an allografted syngeneic mouse tumor model

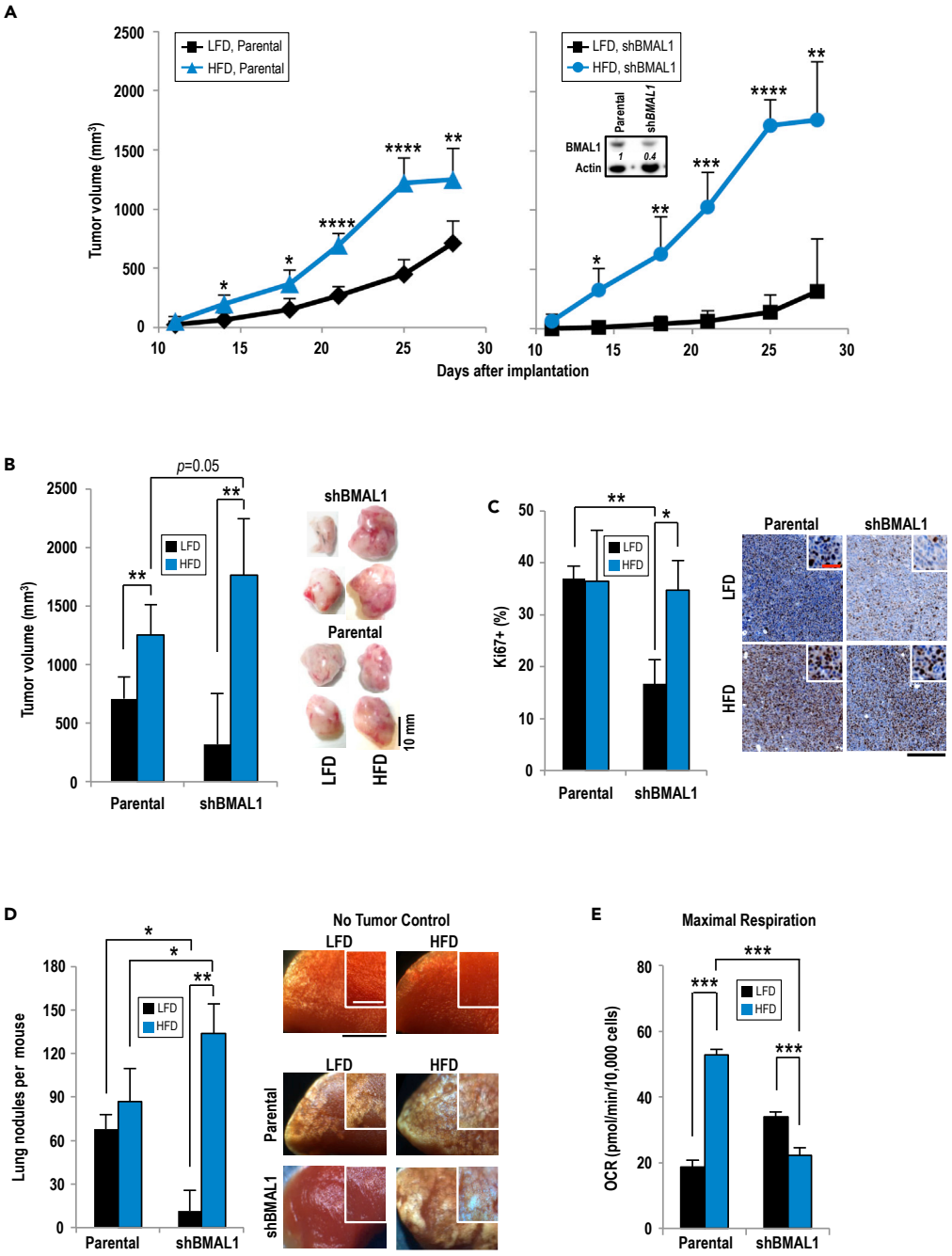

Figure 3. BMAL1 Suppresses HFD-Promoted Tumor Growth

(A) Palpable parental (left panel) or shBMAL1 (right panel) tumors were measured in LFD- and HFD-fed mice. n = 4–6; independent samples' t test at each time point. Inset features immunoblot analysis of parental E0771 and E0771 with stable knockdown of BMAL1. Italicized numbers indicate relative BMAL1 expression level.

(B) Tumor volumes from parental and BMAL1-knockdown E0771 cells in LFD- and HFD-fed mice were analyzed at day 28 after implantation (left panel). Representative tumor images are shown (right panel). n = 4–6.

(C) Formalin-fixed tissue sections from tumors derived from parental and BMAL1-knockdown E0771 cells in LFD- and HFD-fed mice were stained with anti-Ki67 antibody. % Ki67+ cells were calculated as Ki67-positive cells divided by total cells (left panel). Representative images of stained tumor tissues are shown (right panel). n = 3. Scale bar, 200 μm; red scale bar, 100 μm (inset).

Figure 3. *Continued*

(D) Number of lung nodules of parental or BMAL1-knockdown E0771 cells per mouse were counted in LFD- and HFD-fed mice (left panel). Representative image of lung lobes with metastatic nodules are shown (right panel); black scale bar, 3 mm; white scale bar in inset, 2 mm. n ≥ 4.

(E) Relative maximum OCR was calculated for primary E0771 tumors of engrafted cells at passage 2 after extraction from tumors in LFD- and HFD-fed mice. n ≥ 4.

(B–E) Data are shown as mean ± SD; *p < 0.05; **p < 0.01; ***p < 0.001; ****p < 0.0001; one-way ANOVA with Tukey's post hoc. See also Figure S7.

over an MDA-MB-231-xenografted NSG mouse model is that C57BL/6 mice are better responsive to high-fat diet (HFD) feeding (NSG mice are, but only with litter reduction, Behan et al., 2013) and that we are able to study the interaction between cancer cells and their surrounding tumor microenvironment in an immunocompetent animal model. The E0771 cells were derived from a spontaneously developed TNBC in C57BL/6 mice (Ewens et al., 2005; Yang et al., 2017). Parental E0771 cells are poorly metastatic when compared with 4T1 cells (Johnstone et al., 2015) and have homozygous mutations in *Trp53* and *Kras* genes (Yang et al., 2011) with a detectable BMAL1 expression (Figure 3A, inset). When mice reached young adulthood at the age of 8 weeks, they were separated into two groups: HFD or low-fat diet (LFD) (Dutta and Sengupta, 2016). These two diets had equal calories and sucrose for consistent chow palatability and to ensure consistent caloric intake. HFD comprised 60% fat, whereas LFD had 10%. Fasting insulin and glucose levels were measured before starting the diets and 4 weeks after consuming either HFD or LFD. The results showed that LFD did not cause a notable change in fat mass and fasting insulin levels compared with measurements before starting the diet; however, both increased in HFD-fed mice without affecting fasting glucose levels (Figure S7B). To test whether the lack of hyperglycemia in HFD-fed mice is due to hyperinsulinemia, which mimics pre-diabetic state, an oral glucose tolerance test was performed. Following glucose feeding after a starvation period, blood glucose levels spiked faster and remained high longer in HFD-fed mice compared with the mice with LFD (Figure S7C). The HFD-fed mice also displayed higher body weight gained than LFD-fed mice, even though food intake did not differ (Figures S7D and S7E).

After confirming HFD-induced obesity/hyperinsulinemia, the fourth mammary fat pad on the right side of lean or obese mice was implanted with parental E0771 cells or E0771 cells with stable BMAL1 knockdown. The mice were maintained on their respective diet for an additional 4 weeks. In general, HFD accelerated tumor progression over LFD (Figure 3A). Upon tumor harvest, BMAL1-knockdown E0771 tumors were not significantly different in size from parental tumors in lean mice, whereas they were larger than the corresponding tumors of parental cells in hyperinsulinemic mice (Figure 3B). The E0771/shBMAL1-derived tumors from HFD-fed mice showed the largest sizes among these four groups (Figure 3B, right panel). There was no notable difference in Ki67, a marker for cell proliferation, signals between tumors from the parental E0771 cells of LFD- and HFD-fed mice; however, BMAL1 knockdown decreased Ki67 signals in tumors harvested from lean, but not hyperinsulinemic, obese mice (Figure 3C). E0771/shBMAL1-derived tumors from LFD-fed mice had the least proliferative potential. We next examined whole lungs from obese and lean tumor-harboring mice as lungs are a common site of metastasis from E0771-derived mammary tumors (Yousefi et al., 2018). Likewise, the obese tumor-bearing mice harbored more lung tumor nodules than the lean group (Figure 3D). In addition, BMAL1knockdown decreased the lung tumor nodules in LFD-fed tumor-bearing mice, yet significantly increased it in HFD-fed mice. Altogether, BMAL1 serves a non-canonical role of BMAL1 to suppress tumor progression and/or metastasis under hyperinsulinemic obese context.

Last, primary tumor cells from the orthotopically engrafted E0771 tumors were isolated, cultured, and assessed for mitochondrial respiratory function. It is important to note that, recapitulating findings in MDA-MB-231 cells *in vitro*, BMAL1 knockdown increased OCR in E0771 cells recovered from tumors of lean mice, whereas BMAL1 knockdown decreased OCR in E0771 cells from hyperinsulinemic obese mice (Figure 3E). This observation validates the importance of the combined effect of BMAL1-mediated metabolic adaptation and hyperinsulinemia as a determinant of TNBC progression and aggressiveness. In addition, using two different knockdown approaches in cells from two different species yielded comparable conclusion about the role of BMAL1 on mitochondrial bioenergetics, and these separate approaches likely ruled out potential off-target effect(s) of BMAL1 knockdown.

BMAL1 Influences Tumor Microenvironment in Hyperinsulinemic Obese Mice

To further explore how BMAL1 and HFD-induced obesity interactively regulate tumor progression, we examined how the tumor was influenced by the microenvironment. Infiltration of F4/80 macrophage, a

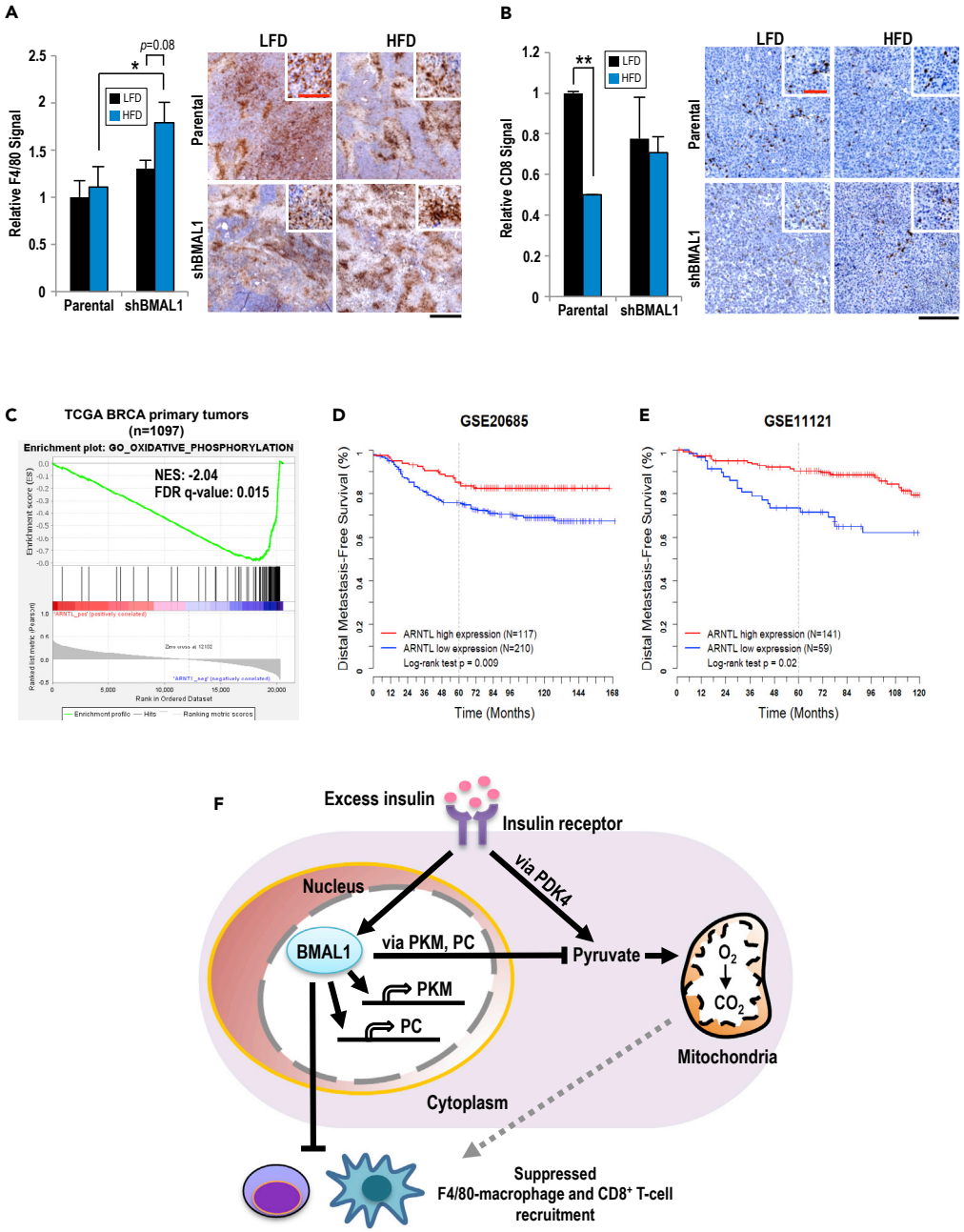

Figure 4. Tumor-Expressed BMAL1 Influences Immune Cell Infiltration

(A) F4/80 signal was quantified as the average area of F4/80 staining in non-overlapping sections of entire tumor and compared with other samples at the same magnification. n = 4 (left panel). Representative images of tissue sections are shown (right panel). Scale bar, 500 μm. Red scale bar, 125 μm (inset).

(B) CD8 signal was quantified as the average area of CD8 staining in non-overlapping sections of entire tumor section and compared with other samples at the same magnification. n = 4. (A and B) Data shown as mean ± SEM; *p < 0.05; **p < 0.01; one-way ANOVA with Tukey's post hoc. Representative images of stained tissue are shown (right panel). Scale bar, 250 μm. Red scale bar, 100 μm (inset).

(C) Gene Set Enrichment Analysis shows that expression of hallmark OxPhos gene set in TCGA BC primary tumors (n = 1,097) is inversely correlated with BMAL1 expression.

(D and E) Kaplan-Meier curves show distal metastasis-free survival rate of patients selected according to BMAL1 expression from two independent datasets GEO: GSE20685 (D) and GSE11121 (E).

Figure 4. *Continued*

(F) Hyperinsulinemia and BMAL1 regulate both internal metabolism and external microenvironment of TNBC. The intrinsic metabolism of TNBC reveals that BMAL1 and hyperinsulinemia have parallel yet distinct regulations of pyruvate and mitochondrial metabolism. The external TNBC microenvironment shows that BMAL1 and hyperinsulinemia in concert control immune cell recruitment and infiltration. The dotted line indicates a possible mechanism for immune cell recruitment via mitochondria-induced reactive oxygen species.

major component of the tumor microenvironment, was assessed by immunohistochemistry (Goswami et al., 2017; Hu et al., 2016; Netea-Maier et al., 2018). Inside the parental E0771-derived tumors, there were no notable differences in F4/80 signals regardless of diet; however, the E0771/shBMAL1-derived tumors in the hyperinsulinemic obese mice, compared with lean mice, exhibited significantly increased F4/80 signals (Figure 4A). Other prominent immune cells featured inside tumors are the $CD8^+$ T cells, which play a protective role and are associated with better cancer prognoses and outcomes (Fu and Jiang, 2018). Tumors from hyperinsulinemic obese mice exhibited significantly decreased $CD8^+$ T cell signals in the parental tumors than those in the lean mice (Figure 4B). Notably, there were no differences in $CD8^+$ T cell recruitment in shBMAL1 tumors regardless of diet (Figure 4B).

We further performed Gene Set Enrichment Analysis of human primary breast tumor data from TCGA and found that the oxidative phosphorylation (OxPhos) pathway is significantly upregulated in patient tumors with downregulated *ARNTL* (Figure 4C). Such observation is consistent with our findings of increased OCR during BMAL1 knockdown (Figures S3E and S3F). Together with Figure S1C, our previously reported increase in OxPhos gene expression in TNBC and HER2-enriched BCs (Cheng et al., 2016) could be attributed to decreased *ARNTL* expression. In addition, although the metabolic states were not available, our analyses of two independent public datasets for human BC (Kao et al., 2011; Schmidt et al., 2008) revealed that reduced *ARNTL* expression is associated with worse distal metastasis-free survival (Figures 4D and 4E).

DISCUSSION

Although HFD-induced obesity drives tumor growth through multiple mechanisms (Nunez et al., 2008), our findings support a new paradigm that reduced expression of *ARNTL*, a key component of the circadian clock, accelerates TNBC tumor growth and lung metastasis in an HFD-induced hyperinsulinemic obese context. Virtually, circadian clock disruption is detrimental to metabolic homeostasis in all cells. To underscore the importance of BMAL1 in the adaptation to hyperinsulinemia in BC cells, here we report that in two different TNBC cells in two distinct models, *in vitro* and *in vivo*, BMAL1 loss (BMAL1 crisis) decreases or increases mitochondrial respiration depending on hyperinsulinemia. In parallel, intrinsic BMAL1 oscillation is suppressed by short-term insulin exposure in a mitochondria-dependent manner in MDA-MB-231 cells. We propose a model in which the reduced BMAL1 expression cooperates with HFD-induced hyperinsulinemic obesity to accelerate TNBC tumor progression and lung metastasis through increased mitochondrial fuel flexibility and reshaped recruitment of macrophages and $CD8^+$ T cells (Figure 4F).

Cancer cells exhibit metabolic plasticity, rewiring their metabolism to satisfy the demands of rapid cell proliferation and survival (Ghaffari et al., 2015). Mitochondria comprise a metabolic hub that is responsible for energy production, and also produce building blocks for cell growth by catabolizing glucose, amino acids, and fatty acids. Although we observed that circadian gene expression and mitochondrial activity appear to be interactive and counter-balanced, the detailed underlying mechanism is still not clear. It is plausible that metabolites from the mitochondria directly affect the transcriptional regulation of circadian genes. In addition, post-translational modifications also play a key role in regulating the expression of circadian genes, such as histone acetylation being required at promoters of BMAL1-CLOCK target genes (DiTacchio et al., 2011). Here, we introduce a link between circadian signaling and mitochondrial function by showing that BMAL1 transcriptionally regulates *PKM* expression. It hints that endogenous pyruvate production functions as a linchpin for BMAL1-mediated metabolic adaptations. As such, the combined effect of BMAL1 and hyperinsulinemic obesity on reshaping the tumor microenvironment is conceivably mediated by regulating intracellular pyruvate utilization. Our model on the combined effect of intracellular pyruvate and on promoting tumor progression is supported by reports that pyruvate metabolism is important in maintaining colon cancer stem cell proliferation (Schell et al., 2017) and that PKM2-null mice display increased HFD-induced metabolic stress (Dayton et al., 2016).

Inflammation plays a key role in hyperinsulinemic obesity and metabolic disease (Chawla et al., 2011; Lumeng and Saltiel, 2011). In our model, it appears that cancer cell-intrinsic BMAL1 acts as a critical suppressor

of F4/80 macrophage tumor infiltration under hyperinsulinemic obesity. Cancer cell BMAL1-mediated suppression of F4/80 macrophage infiltration thus has important implications for how anti-tumor immunity is impaired during hyperinsulinemic obesity. A causative role of immune cells in promoting tumor progression has been demonstrated (Wellenstein and de Visser, 2018) as depleting inflammatory immune cells leads to rapid improvement in insulin sensitivity and glucose tolerance, which is associated with decreased local and systemic inflammation in obese mice (Nishimura et al., 2009). The role of BMAL1 in immune cell recruitment is not yet elucidated. The observed decrease in $CD8^+$ T cell recruitment in tumors harvested from HFD-fed mice is in agreement with findings in another report (Wang et al., 2019). Considering such a decrease was not observed in BMAL1-knockdown tumors, one plausible function of BMAL1 is to prevent T cell exhaustion during obesity. Together, these data show that the immune cells surrounding the tumor are likely affected by the tumor cells' metabolic flexibility. Cancer-associated fibroblasts have been shown to secrete pyruvate to support metabolism in the tumor (Sakamoto et al., 2019) and the BMAL1-suppressed pyruvate utilization we observed in CIT cells may contribute to the tumor microenvironment landscape. Furthermore, macrophages consume exogenous pyruvate, resulting in increased PD-L1 expression and suppressed anti-tumor immune cells (Watanabe et al., 2017), providing a plausible mechanism of tumor-secreted pyruvate and uptake by immune cells.

In summary, our experimental results showed that BMAL1 suppresses TNBC progression in multiple ways: by maintaining the clock machinery and circadian rhythms, by suppressing hyperinsulinemia-dysregulated mitochondrial activity and pyruvate utilization, and by suppressing pro-inflammatory components of the immune microenvironment in the obese context. The latter roles could be attributed to non-canonical circadian functions of BMAL1. In this context, our results provide a compelling case for BMAL1 expression to be examined in patients with TNBC who also present with hyperinsulinemia in the clinic. TNBC tumors with BMAL1 crisis are predicted to have worse outcomes, especially during obesity/hyperinsulinemia. BMAL1 appears to act as a tumor suppressor in TNBC during obesity/hyperinsulinemia, underscoring the importance of understanding BMAL1-mediated mitochondrial metabolic reprogramming during CIT adaptation, which could be exploited pharmacologically or with diet management for better patient outcomes in the future.

Limitations of the Study

There is ample evidence that the cellular circadian clock regulates more than just cell-intrinsic metabolic processes. Based on consistent observations using two distinct models of TNBC, both *in vitro* and *in vivo*, we propose a paradigm that BMAL1 serves as a metabolic switch on hyperinsulinemia-regulated mitochondrial activity to govern TNBC tumor progression. Indeed, there is a need to better link circadian biology to cancer risk. Although our findings provide insights regarding the non-canonical BMAL1 function, additional studies are needed to validate how BMAL1 loss (BMAL1 crisis) influences most cases of BC in different metabolic states and whether these insights can be leveraged into an effective therapy. Also, although we demonstrated that BMAL1 crisis confers advantages to cancer cells in both intrinsic metabolism and extrinsic inflammatory microenvironment during hyperinsulinemia, the underlying signaling mechanism among BMAL1 crisis, hyperinsulinemia, and tumorigenesis *in vivo* remains to be established.

METHODS

All methods can be found in the accompanying Transparent Methods supplemental file.

SUPPLEMENTAL INFORMATION

Supplemental Information can be found online at https://doi.org/10.1016/j.isci.2020.100839.

ACKNOWLEDGMENTS

We thank the members of Dr. Ann's laboratory and Drs. Rama Natarajan and Lei Jiang for helpful discussions on the manuscript. We thank Dr. Joe Gray (Oregon Health & Science University) for providing breast cancer cell line gene expression data. This work was supported in part by funds from the National Cancer Institute of United States grant R01CA220693 (D.K.A. and V.L.S.), Department of Defense of United States grant BC141351 (M.A.L.), City of Hope Center for Cancer and Aging predoctoral fellowship (C.A.R.), and P30CA033572 (supporting research work carried out at City of Hope Core Facilities).

AUTHOR CONTRIBUTIONS

Conceptualization, C.A.R. and D.K.A.; Methodology, C.A.R., C.O., Y.C., V.L.S., and D.K.A.; Investigation, C.A.R., C.O., Y.Q., Y.C., and C.-T.C.; Data analysis, C.A.R., C.O., Y.Q., and Y.C.; Resources, M.A.L. and D.K.A.; Manuscript Writing, C.A.R, C.O., Y.Q., M.A.L., V.L.S., and D.K.A.; Funding Acquisition, C.A.R., M.A.L., V.L.S., and D.K.A.

DECLARATION OF INTERESTS

The authors declare no competing interests.

Received: June 20, 2019
Revised: September 3, 2019
Accepted: January 9, 2020
Published: February 21, 2020

REFERENCES

Balsalobre, A., Damiola, F., and Schibler, U. (1998). A serum shock induces circadian gene expression in mammalian tissue culture cells. Cell *93*, 929–937.

Behan, J.W., Ehsanipour, E.A., Sheng, X., Pramanik, R., Wang, X., Hsieh, Y.T., Kim, Y.M., and Mittelman, S.D. (2013). Activation of adipose tissue macrophages in obese mice does not require lymphocytes. Obesity *21*, 1380–1388.

Bell-Pedersen, D., Cassone, V.M., Earnest, D.J., Golden, S.S., Hardin, P.E., Thomas, T.L., and Zoran, M.J. (2005). Circadian rhythms from multiple oscillators: lessons from diverse organisms. Nat. Rev. Genet. *6*, 544–556.

Blakeman, V., Williams, J.L., Meng, Q.J., and Streuli, C.H. (2016). Circadian clocks and breast cancer. Breast Cancer Res. *18*, 89.

Breit, A., Miek, L., Schredelseker, J., Geibel, M., Merrow, M., and Gudermann, T. (2018). Insulin-like growth factor-1 acts as a zeitgeber on hypothalamic circadian clock gene expression via glycogen synthase kinase-3beta signaling. J. Biol. Chem. *293*, 17278–17290.

Bunger, M.K., Wilsbacher, L.D., Moran, S.M., Clendenin, C., Radcliffe, L.A., Hogenesch, J.B., Simon, M.C., Takahashi, J.S., and Bradfield, C.A. (2000). Mop3 is an essential component of the master circadian pacemaker in mammals. Cell *103*, 1009–1017.

Capasso, I., Esposito, E., de Laurentiis, M., Maurea, N., Cavalcanti, E., Botti, G., Petrillo, A., Montella, M., D'Aiuto, M., Coppola, C., et al. (2014). Metabolic syndrome-breast cancer link varies by intrinsic molecular subtype. Diabetol. Metab. Syndr. *6*, 105.

Cederroth, C.R., Albrecht, U., Bass, J., Brown, S.A., Dyhrfjeld-Johnsen, J., Gachon, F., Green, C.B., Hastings, M.H., Helfrich-Forster, C., Hogenesch, J.B., et al. (2019). Medicine in the fourth dimension. Cell Metab. *30*, 238–250.

Chawla, A., Nguyen, K.D., and Goh, Y.P. (2011). Macrophage-mediated inflammation in metabolic disease. Nat. Rev. Immunol. *11*, 738–749.

Cheng, C.T., Kuo, C.Y., Ouyang, C., Li, C.F., Chung, Y., Chan, D.C., Kung, H.J., and Ann, D.K. (2016). Metabolic stress-induced phosphorylation of KAP1 Ser473 blocks mitochondrial fusion in breast cancer cells. Cancer Res. *76*, 5006–5018.

Dang, F., Sun, X., Ma, X., Wu, R., Zhang, D., Chen, Y., Xu, Q., Wu, Y., and Liu, Y. (2016). Insulin post-transcriptionally modulates Bmal1 protein to affect the hepatic circadian clock. Nat. Commun. *7*, 12696.

Davis, S., Mirick, D.K., and Stevens, R.G. (2001). Night shift work, light at night, and risk of breast cancer. J. Natl. Cancer Inst. *93*, 1557–1562.

Dayton, T.L., Gocheva, V., Miller, K.M., Israelsen, W.J., Bhutkar, A., Clish, C.B., Davidson, S.M., Luengo, A., Bronson, R.T., Jacks, T., et al. (2016). Germline loss of PKM2 promotes metabolic distress and hepatocellular carcinoma. Genes Dev. *30*, 1020–1033.

de Assis, L.V.M., Kinker, G.S., Moraes, M.N., Markus, R.P., Fernandes, P.A., and Castrucci, A.M.L. (2018). Expression of the circadian clock gene BMAL1 positively correlates with antitumor immunity and patient survival in metastatic melanoma. Front. Oncol. *8*, 185.

Del Giudice, M.E., Fantus, I.G., Ezzat, S., McKeown-Eyssen, G., Page, D., and Goodwin, P.J. (1998). Insulin and related factors in premenopausal breast cancer risk. Breast Cancer Res. Treat. *47*, 111–120.

Deng, W., Zhu, S., Zeng, L., Liu, J., Kang, R., Yang, M., Cao, L., Wang, H., Billiar, T.R., Jiang, J., et al. (2018). The circadian clock controls immune checkpoint pathway in sepsis. Cell Rep. *24*, 366–378.

DiTacchio, L., Le, H.D., Vollmers, C., Hatori, M., Witcher, M., Secombe, J., and Panda, S. (2011). Histone lysine demethylase JARID1a activates CLOCK-BMAL1 and influences the circadian clock. Science *333*, 1881–1885.

Dutta, S., and Sengupta, P. (2016). Men and mice: relating their ages. Life Sci. *152*, 244–248.

Ewens, A., Mihich, E., and Ehrke, M.J. (2005). Distant metastasis from subcutaneously grown E0771 medullary breast adenocarcinoma. Anticancer Res. *25*, 3905–3915.

Fu, C., and Jiang, A. (2018). Dendritic cells and CD8 T cell immunity in tumor microenvironment. Front. Immunol. *9*, 3059.

Garcia-Estevez, L., and Moreno-Bueno, G. (2019). Updating the role of obesity and cholesterol in breast cancer. Breast Cancer Res. *21*, 35.

Ghaffari, P., Mardinoglu, A., and Nielsen, J. (2015). Cancer metabolism: a modeling perspective. Front. Physiol. *6*, 382.

Goodwin, P.J., Ennis, M., Pritchard, K.I., Trudeau, M.E., Koo, J., Madarnas, Y., Hartwick, W., Hoffman, B., and Hood, N. (2002). Fasting insulin and outcome in early-stage breast cancer: results of a prospective cohort study. J. Clin. Oncol. *20*, 42–51.

Goswami, K.K., Ghosh, T., Ghosh, S., Sarkar, M., Bose, A., and Baral, R. (2017). Tumor promoting role of anti-tumor macrophages in tumor microenvironment. Cell. Immunol. *316*, 1–10.

Gunter, M.J., Hoover, D.R., Yu, H., Wassertheil-Smoller, S., Rohan, T.E., Manson, J.E., Li, J., Ho, G.Y., Xue, X., Anderson, G.L., et al. (2009). Insulin, insulin-like growth factor-I, and risk of breast cancer in postmenopausal women. J. Natl. Cancer Inst. *101*, 48–60.

Hanahan, D., and Weinberg, R.A. (2011). Hallmarks of cancer: the next generation. Cell *144*, 646–674.

Hatanaka, F., Matsubara, C., Myung, J., Yoritaka, T., Kamimura, N., Tsutsumi, S., Kanai, A., Suzuki, Y., Sassone-Corsi, P., Aburatani, H., et al. (2010). Genome-wide profiling of the core clock protein BMAL1 targets reveals a strict relationship with metabolism. Mol. Cell. Biol. *30*, 5636–5648.

Hu, W., Li, X., Zhang, C., Yang, Y., Jiang, J., and Wu, C. (2016). Tumor-associated macrophages in cancers. Clin. Transl. Oncol. *18*, 251–258.

Hursting, S.D., Digiovanni, J., Dannenberg, A.J., Azrad, M., Leroith, D., Demark-Wahnefried, W., Kakarala, M., Brodie, A., and Berger, N.A. (2012). Obesity, energy balance, and cancer: new opportunities for prevention. Cancer Prev. Res. *5*, 1260–1272.

Jacobi, D., Liu, S., Burkewitz, K., Kory, N., Knudsen, N.H., Alexander, R.K., Unluturk, U., Li, X., Kong, X., Hyde, A.L., et al. (2015). Hepatic Bmal1 regulates rhythmic mitochondrial dynamics and promotes metabolic fitness. Cell Metab. *22*, 709–720.

Johnstone, C.N., Smith, Y.E., Cao, Y., Burrows, A.D., Cross, R.S., Ling, X., Redvers, R.P., Doherty, J.P., Eckhardt, B.L., Natoli, A.L., et al. (2015). Functional and molecular characterisation of EO771.LMB tumours, a new C57BL/6-mouse-derived model of spontaneously metastatic mammary cancer. Dis. Model. Mech. *8*, 237–251.

Kao, K.J., Chang, K.M., Hsu, H.C., and Huang, A.T. (2011). Correlation of microarray-based breast cancer molecular subtypes and clinical outcomes: implications for treatment optimization. BMC Cancer *11*, 143.

Lawlor, D.A., Smith, G.D., and Ebrahim, S. (2004). Hyperinsulinaemia and increased risk of breast cancer: findings from the British Women's Heart and Health Study. Cancer Causes Control *15*, 267–275.

Lesicka, M., Jablonska, E., Wieczorek, E., Seroczynska, B., Siekierzycka, A., Skokowski, J., Kalinowski, L., Wasowicz, W., and Reszka, E. (2018). Altered circadian genes expression in breast cancer tissue according to the clinical characteristics. PLoS One *13*, e0199622.

Lin, H.H., and Farkas, M.E. (2018). Altered circadian rhythms and breast cancer: from the human to the molecular level. Front. Endocrinol. *9*, 219.

Lipscombe, L.L., Goodwin, P.J., Zinman, B., McLaughlin, J.R., and Hux, J.E. (2006). Increased prevalence of prior breast cancer in women with newly diagnosed diabetes. Breast Cancer Res. Treat. *98*, 303–309.

Liu, J., Zhou, B., Yan, M., Huang, R., Wang, Y., He, Z., Yang, Y., Dai, C., Wang, Y., Zhang, F., et al. (2016). CLOCK and BMAL1 regulate muscle insulin sensitivity via SIRT1 in male mice. Endocrinology *157*, 2259–2269.

Luciano, A.K., Zhou, W., Santana, J.M., Kyriakides, C., Velazquez, H., and Sessa, W.C. (2018). CLOCK phosphorylation by AKT regulates its nuclear accumulation and circadian gene expression in peripheral tissues. J. Biol. Chem. *293*, 9126–9136.

Lumeng, C.N., and Saltiel, A.R. (2011). Inflammatory links between obesity and metabolic disease. J. Clin. Invest. *121*, 2111–2117.

Luo, Q., Xiao, Y., Alex, A., Cummins, T.R., and Bhatwadekar, A.D. (2019). The diurnal rhythm of insulin receptor substrate-1 (IRS-1) and Kir4.1 in diabetes: implications for a clock gene Bmal1. Invest. Ophthalmol. Vis. Sci. *60*, 1928–1936.

Marcheva, B., Ramsey, K.M., Buhr, E.D., Kobayashi, Y., Su, H., Ko, C.H., Ivanova, G., Omura, C., Mo, S., Vitaterna, M.H., et al. (2010). Disruption of the clock components CLOCK and BMAL1 leads to hypoinsulinaemia and diabetes. Nature *466*, 627–631.

Mayer, M.J., Klotz, L.H., and Venkateswaran, V. (2015). Metformin and prostate cancer stem cells: a novel therapeutic target. Prostate Cancer Prostatic Dis. *18*, 303–309.

McGinnis, G.R., Tang, Y., Brewer, R.A., Brahma, M.K., Stanley, H.L., Shanmugam, G., Rajasekaran, N.S., Rowe, G.C., Frank, S.J., Wende, A.R., et al. (2017). Genetic disruption of the cardiomyocyte circadian clock differentially influences insulin-mediated processes in the heart. J. Mol. Cell. Cardiol. *110*, 80–95.

Nakahata, Y., Sahar, S., Astarita, G., Kaluzova, M., and Sassone-Corsi, P. (2009). Circadian control of the NAD+ salvage pathway by CLOCK-SIRT1. Science *324*, 654–657.

Netea-Maier, R.T., Smit, J.W.A., and Netea, M.G. (2018). Metabolic changes in tumor cells and tumor-associated macrophages: a mutual relationship. Cancer Lett. *413*, 102–109.

Nishimura, S., Manabe, I., Nagasaki, M., Eto, K., Yamashita, H., Ohsugi, M., Otsu, M., Hara, K., Ueki, K., Sugiura, S., et al. (2009). CD8+ effector T cells contribute to macrophage recruitment and adipose tissue inflammation in obesity. Nat. Med. *15*, 914–920.

Nunez, N.P., Perkins, S.N., Smith, N.C., Berrigan, D., Berendes, D.M., Varticovski, L., Barrett, J.C., and Hursting, S.D. (2008). Obesity accelerates mouse mammary tumor growth in the absence of ovarian hormones. Nutr. Cancer *60*, 534–541.

Pan, X., Bradfield, C.A., and Hussain, M.M. (2016). Global and hepatocyte-specific ablation of Bmal1 induces hyperlipidaemia and enhances atherosclerosis. Nat. Commun. *7*, 13011.

Papagiannakopoulos, T., Bauer, M.R., Davidson, S.M., Heimann, M., Subbaraj, L., Bhutkar, A., Bartlebaugh, J., Vander Heiden, M.G., and Jacks, T. (2016). Circadian rhythm disruption promotes lung tumorigenesis. Cell Metab. *24*, 324–331.

Partch, C.L., Green, C.B., and Takahashi, J.S. (2014). Molecular architecture of the mammalian circadian clock. Trends Cell Biol. *24*, 90–99.

Perou, C.M., Sorlie, T., Eisen, M.B., van de Rijn, M., Jeffrey, S.S., Rees, C.A., Pollack, J.R., Ross, D.T., Johnsen, H., Akslen, L.A., et al. (2000). Molecular portraits of human breast tumours. Nature *406*, 747–752.

Perry, R.J., Camporez, J.G., Kursawe, R., Titchenell, P.M., Zhang, D., Perry, C.J., Jurczak, M.J., Abudukadier, A., Han, M.S., Zhang, X.M., et al. (2015). Hepatic acetyl CoA links adipose tissue inflammation to hepatic insulin resistance and type 2 diabetes. Cell *160*, 745–758.

Petan, T., Jarc, E., and Jusovic, M. (2018). Lipid droplets in cancer: guardians of fat in a stressful world. Molecules *23*, 1941.

Rambold, A.S., Cohen, S., and Lippincott-Schwartz, J. (2015). Fatty acid trafficking in starved cells: regulation by lipid droplet lipolysis, autophagy, and mitochondrial fusion dynamics. Dev. Cell *32*, 678–692.

Ramsey, K.M., Yoshino, J., Brace, C.S., Abrassart, D., Kobayashi, Y., Marcheva, B., Hong, H.K., Chong, J.L., Buhr, E.D., Lee, C., et al. (2009). Circadian clock feedback cycle through NAMPT-mediated NAD+ biosynthesis. Science *324*, 651–654.

Rey, G., Cesbron, F., Rougemont, J., Reinke, H., Brunner, M., and Naef, F. (2011). Genome-wide and phase-specific DNA-binding rhythms of BMAL1 control circadian output functions in mouse liver. PLoS Biol. *9*, e1000595.

Sahar, S., and Sassone-Corsi, P. (2009). Metabolism and cancer: the circadian clock connection. Nat. Rev. Cancer *9*, 886–896.

Sakamoto, A., Kunou, S., Shimada, K., Tsunoda, M., Aoki, T., Iriyama, C., Tomita, A., Nakamura, S., Hayakawa, F., and Kiyoi, H. (2019). Pyruvate secreted from patient-derived cancer-associated fibroblasts supports survival of primary lymphoma cells. Cancer Sci. *110*, 269–278.

Sato, T.K., Yamada, R.G., Ukai, H., Baggs, J.E., Miraglia, L.J., Kobayashi, T.J., Welsh, D.K., Kay, S.A., Ueda, H.R., and Hogenesch, J.B. (2006). Feedback repression is required for mammalian circadian clock function. Nat. Genet. *38*, 312–319.

Schell, J.C., Wisidagama, D.R., Bensard, C., Zhao, H., Wei, P., Tanner, J., Flores, A., Mohlman, J., Sorensen, L.K., Earl, C.S., et al. (2017). Control of intestinal stem cell function and proliferation by mitochondrial pyruvate metabolism. Nat. Cell Biol. *19*, 1027–1036.

Schernhammer, E.S., Laden, F., Speizer, F.E., Willett, W.C., Hunter, D.J., Kawachi, I., and Colditz, G.A. (2001). Rotating night shifts and risk of breast cancer in women participating in the nurses' health study. J. Natl. Cancer Inst. *93*, 1563–1568.

Schmidt, M., Bohm, D., von Torne, C., Steiner, E., Puhl, A., Pilch, H., Lehr, H.A., Hengstler, J.G., Kolbl, H., and Gehrmann, M. (2008). The humoral immune system has a key prognostic impact in node-negative breast cancer. Cancer Res. *68*, 5405–5413.

Subik, K., Lee, J.F., Baxter, L., Strzepek, T., Costello, D., Crowley, P., Xing, L., Hung, M.C., Bonfiglio, T., Hicks, D.G., et al. (2010). The expression patterns of ER, PR, HER2, CK5/6, EGFR, Ki-67 and AR by immunohistochemical analysis in breast cancer cell lines. Breast Cancer *4*, 35–41.

Tang, Q., Cheng, B., Xie, M., Chen, Y., Zhao, J., Zhou, X., and Chen, L. (2017). Circadian clock gene Bmal1 inhibits tumorigenesis and increases paclitaxel sensitivity in tongue squamous cell carcinoma. Cancer Res. *77*, 532–544.

Toft, D.J., and Cryns, V.L. (2011). Minireview: basal-like breast cancer: from molecular profiles to targeted therapies. Mol. Endocrinol. *25*, 199–211.

Tsujimoto, T., Kajio, H., and Sugiyama, T. (2017). Association between hyperinsulinemia and increased risk of cancer death in nonobese and obese people: a population-based observational study. Int. J. Cancer *141*, 102–111.

Verlande, A., and Masri, S. (2019). Circadian clocks and cancer: timekeeping governs cellular metabolism. Trends Endocrinol. Metab. *30*, 445–458.

Wang, Z., Aguilar, E.G., Luna, J.I., Dunai, C., Khuat, L.T., Le, C.T., Mirsoian, A., Minnar, C.M., Stoffel, K.M., Sturgill, I.R., et al. (2019). Paradoxical effects of obesity on T cell function during tumor progression and PD-1 checkpoint blockade. Nat. Med. *25*, 141–151.

Watanabe, R., Shirai, T., Namkoong, H., Zhang, H., Berry, G.J., Wallis, B.B., Schaefgen, B., Harrison, D.G., Tremmel, J.A., Giacomini, J.C., et al. (2017). Pyruvate controls the checkpoint inhibitor PD-L1 and suppresses T cell immunity. J. Clin. Invest. *127*, 2725–2738.

Wegrzyn, L.R., Tamimi, R.M., Rosner, B.A., Brown, S.B., Stevens, R.G., Eliassen, A.H., Laden, F., Willett, W.C., Hankinson, S.E., and Schernhammer, E.S. (2017). Rotating night-shift work and the risk of breast cancer in the nurses' health studies. Am. J. Epidemiol. *186*, 532–540.

Wellenstein, M.D., and de Visser, K.E. (2018). Cancer-cell-intrinsic mechanisms shaping the tumor immune landscape. Immunity *48*, 399–416.

Yang, X.R., Chang-Claude, J., Goode, E.L., Couch, F.J., Nevanlinna, H., Milne, R.L., Gaudet, M., Schmidt, M.K., Broeks, A., Cox, A., et al. (2011). Associations of breast cancer risk factors with tumor subtypes: a pooled analysis from the Breast Cancer Association Consortium studies. J. Natl. Cancer Inst. *103*, 250–263.

Yang, Y., Yang, H.H., Hu, Y., Watson, P.H., Liu, H., Geiger, T.R., Anver, M.R., Haines, D.C., Martin, P., Green, J.E., et al. (2017). Immunocompetent mouse allograft models for development of therapies to target breast cancer metastasis. Oncotarget *8*, 30621–30643.

Ye, Y., Xiang, Y., Ozguc, F.M., Kim, Y., Liu, C.J., Park, P.K., Hu, Q., Diao, L., Lou, Y., Lin, C., et al. (2018). The genomic landscape and pharmacogenomic interactions of clock genes in cancer chronotherapy. Cell Syst. *6*, 314–328.e2.

Yoo, S.H., Yamazaki, S., Lowrey, P.L., Shimomura, K., Ko, C.H., Buhr, E.D., Siepka, S.M., Hong, H.K., Oh, W.J., Yoo, O.J., et al. (2004). PERIOD2::LUCIFERASE real-time reporting of circadian dynamics reveals persistent circadian oscillations in mouse peripheral tissues. Proc. Natl. Acad. Sci. U S A *101*, 5339–5346.

Yousefi, M., Nosrati, R., Salmaninejad, A., Dehghani, S., Shahryari, A., and Saberi, A. (2018). Organ-specific metastasis of breast cancer: molecular and cellular mechanisms underlying lung metastasis. Cell. Oncol. *41*, 123–140.

Zhang, D.Q., Tong, X., Arthurs, B., Guha, A., Rui, L.Y., Kamath, A., Inoki, K., and Yin, L. (2014). Liver clock protein BMAL1 promotes de novo lipogenesis through insulin-mTORC2-AKT signaling. J. Biol. Chem. *289*, 25925–25935.

iScience, Volume *23*

Supplemental Information

A Non-canonical Function of BMAL1 Metabolically Limits Obesity-Promoted Triple-Negative Breast Cancer

Cassandra A. Ramos, Ching Ouyang, Yue Qi, Yiyin Chung, Chun-Ting Cheng, Mark A. LaBarge, Victoria L. Seewaldt, and David K. Ann

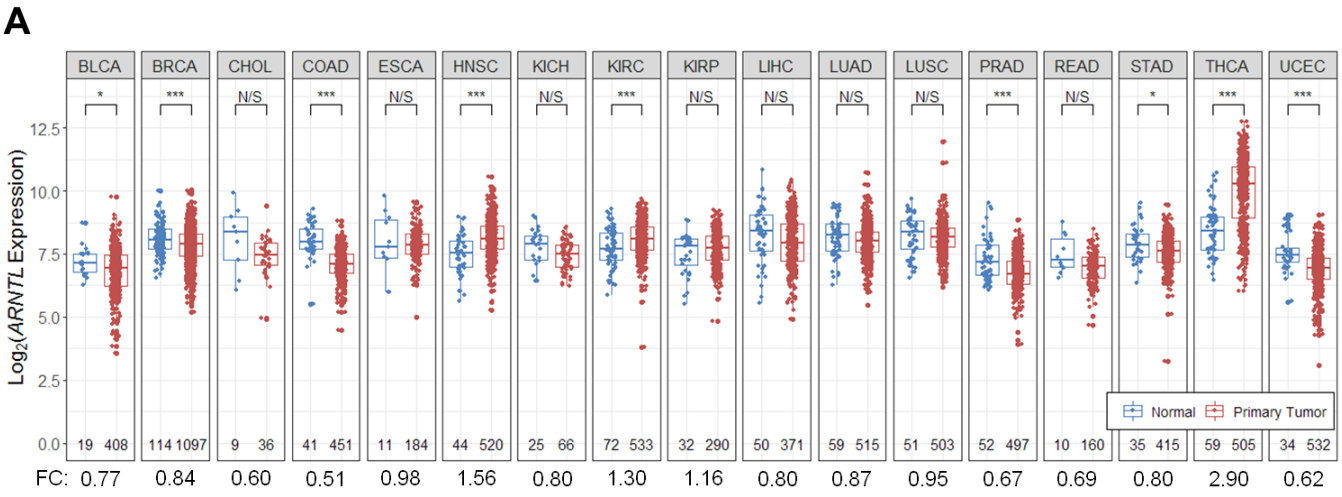
A
BLCA
BRCA
CHOL
COAD
ESCA
HNSC
KICH
KIRC
KIRP
LIHC
LUAD
LUSC
PRAD
READ
STAD
THCA
UCEC
Log2(ARNTL Expression)
Normal
Primary Tumor
FC: 0.77 0.84 0.60 0.51 0.98 1.56 0.80 1.30 1.16 0.80 0.87 0.95 0.67 0.69 0.80 2.90 0.62

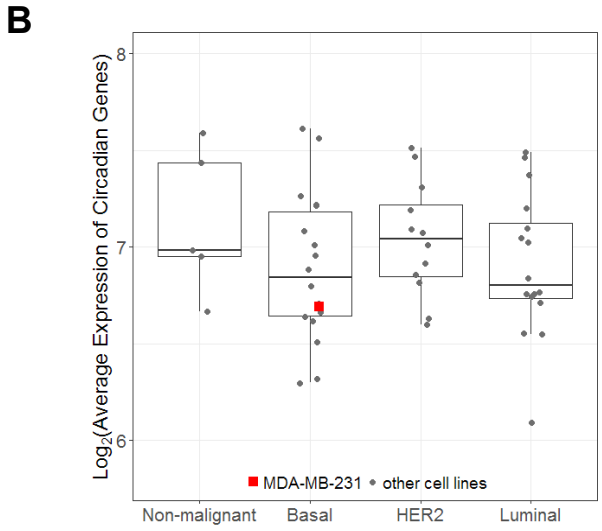
B
Log2(Average Expression of Circadian Genes)
MDA-MB-231
other cell lines
Non-malignant
Basal
HER2
Luminal

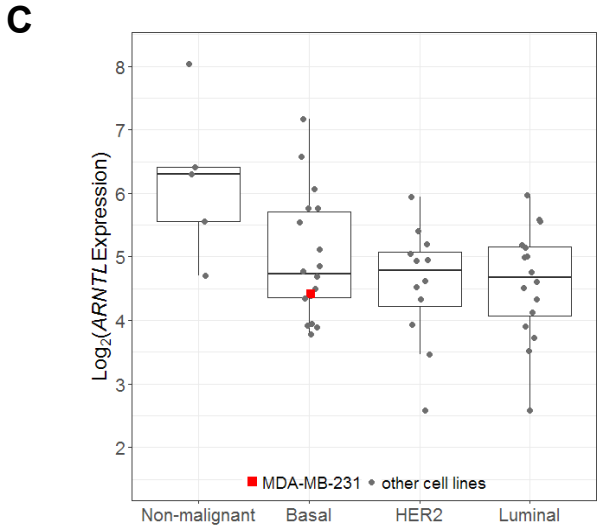
C
Log2(ARNTL Expression)
MDA-MB-231
other cell lines
Non-malignant
Basal
HER2
Luminal

Figure S1

Figure S1. Expression of core circadian gene *ARNTL* is altered in BC. Related to Figure 1. **(A)** Standard boxplots are applied to visualize the log2-transformed *ARNTL* expression levels (RSEM+1) between normal tissues (blue) and primary tumors (red) across 17 cancer types in TCGA Pan-Cancer study. Cancer types having more than five samples of normal tissues were included in this analysis. The number of samples and fold change (FC) of normalized expression values are labeled at the bottom. Statistical *p*-values between groups were determined by Welch's t-tests. ***: $p<0.001$; **: $p<0.01$; *: $p<0.05$; N/S: $p>0.05$. BLCA: bladder urothelial carcinoma; BRCA: breast invasive carcinoma; CHOL: cholangiocarcinoma; COAD: colon adenocarcinoma; ESCA: Esophageal carcinoma; HNSC: head and neck squamous cell carcinoma; KICH: kidney chromophobe; KIRC: kidney renal clear cell carcinoma; KIRP: kidney renal papillary cell carcinoma; LIHC: liver hepatocellular carcinoma; LUAD: lung adenocarcinoma; LUSC: lung squamous cell carcinoma; PRAD: prostate adenocarcinoma; READ: rectal adenocarcinoma; STAD: Stomach adenocarcinoma; THCA: Thyroid carcinoma; UCEC: uterine corpus endometrial carcinoma. **(B-C)** RNA-seq data from 51 BC cell lines, grouped by BC subtypes, were analyzed for the average expression of circadian genes **(B)** and *ARNTL* **(C)**.

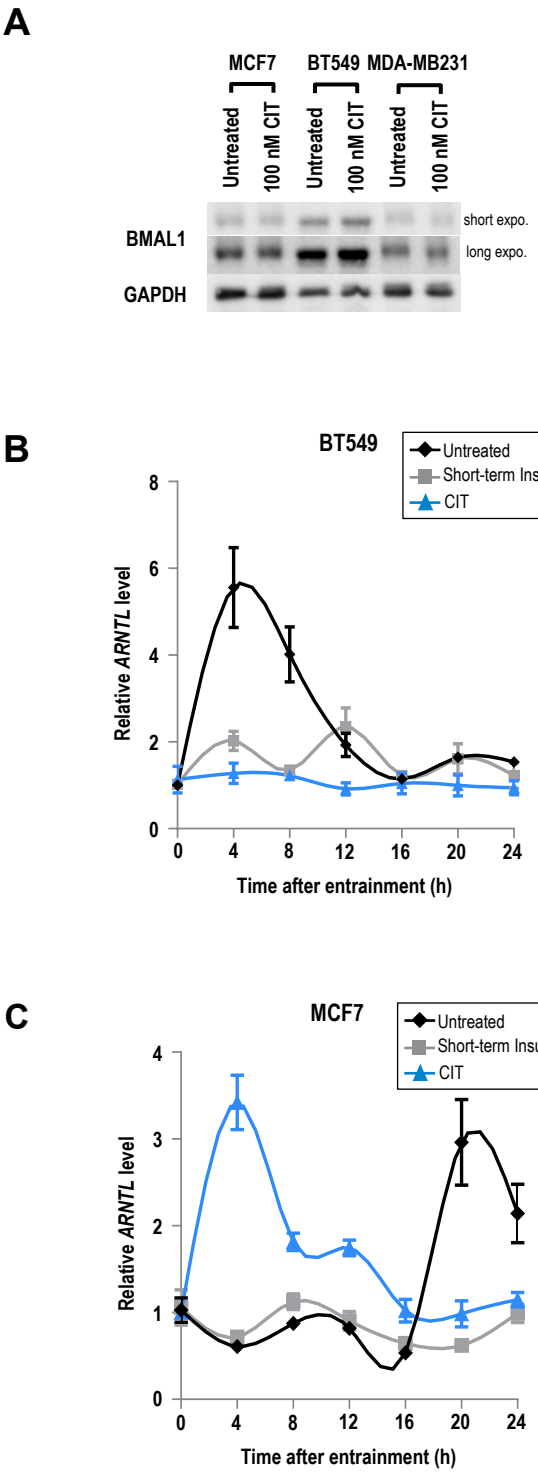
A
MCF7
BT549
MDA-MB231
Untreated
100 nM CIT
Untreated
100 nM CIT
Untreated
100 nM CIT
BMAL1
GAPDH
short expo.
long expo.
B
BT549
Untreated
Short-term Insulin
CIT
Relative ARNTL level
Time after entrainment (h)
C
MCF7
Untreated
Short-term Insulin
CIT
Relative ARNTL level
Time after entrainment (h)

Figure S2

Figure S2. Alteration of *ARNTL* mRNA oscillation upon insulin treatment in BT549 and MCF7 cells. Related to Figure 1. (A) Western blots comparing BMAL1 in MCF7, BT549, and MDA-MB231 cells before (Untreated) and after CIT (at least 10 passages of 100 nM insulin). **(B-C)** *ARNTL* expression in untreated, short-term insulin treated, and CIT BT549 **(B)** and MCF7 cells **(C)**. *ARNTL* mRNA oscillation pattern was analyzed by qRT-PCR after serum shock. After serum shock, cells were kept in DMEM and harvested for total RNA extraction every 4 h. *GAPDH* expression serves as the internal control and *ARNTL* expression of untreated cells at 0 h is set to 1. Data are shown as mean±SD; n=3.

Figure S2 Legend

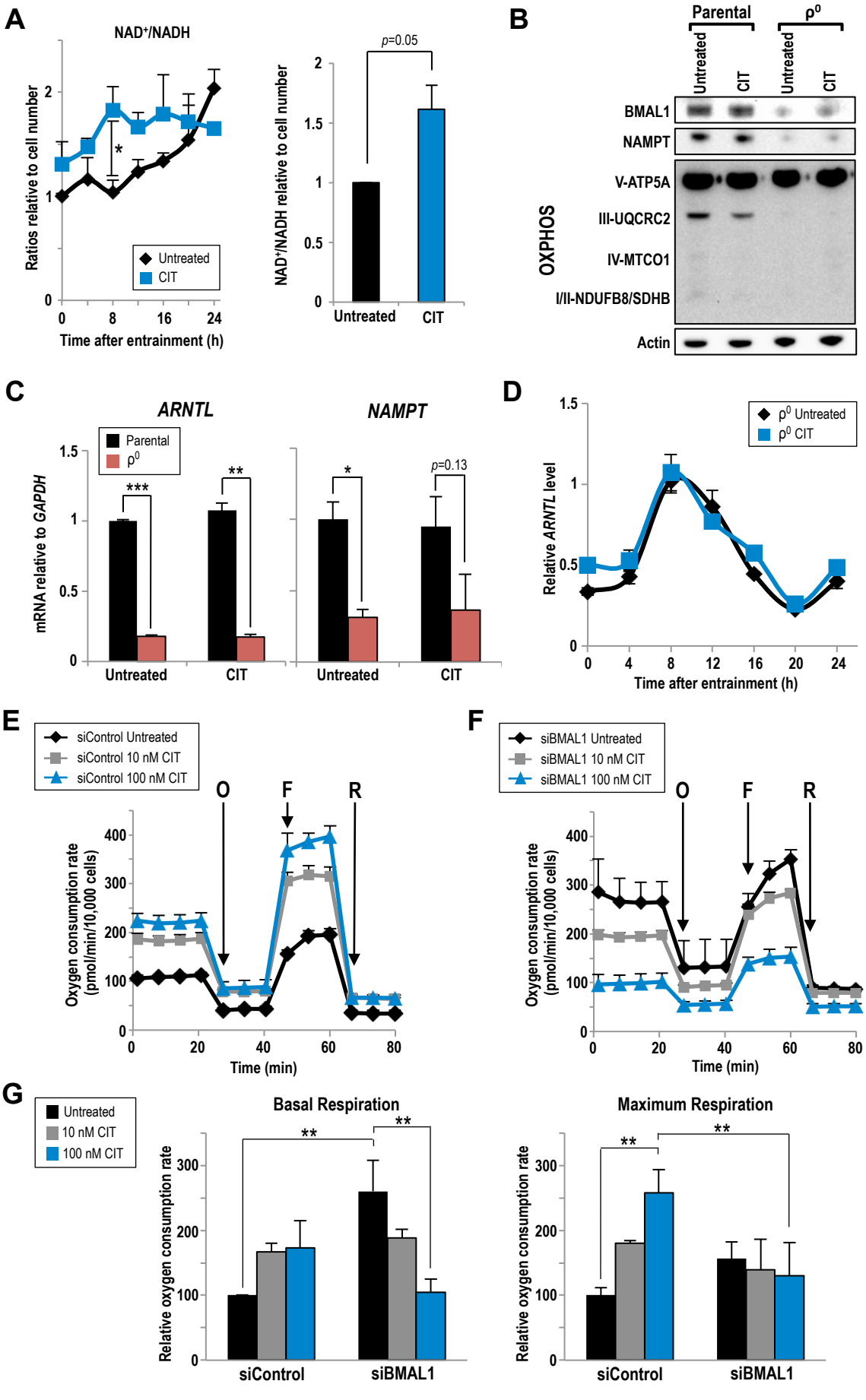
A
NAD+/NADH
Ratios relative to cell number
Time after entrainment (h)
Untreated
CIT
p=0.05
NAD+/NADH relative to cell number
B
Parental
ρ0
Untreated
CIT
BMAL1
NAMPT
V-ATP5A
III-UQCRC2
IV-MTCO1
I/II-NDUFB8/SDHB
OXPHOS
Actin
C
ARNTL
NAMPT
Parental
ρ0
mRNA relative to GAPDH
p=0.13
D
ρ0 Untreated
ρ0 CIT
Relative ARNTL level
Time after entrainment (h)
E
siControl Untreated
siControl 10 nM CIT
siControl 100 nM CIT
O
F
R
Oxygen consumption rate (pmol/min/10,000 cells)
Time (min)
F
siBMAL1 Untreated
siBMAL1 10 nM CIT
siBMAL1 100 nM CIT
G
Untreated
10 nM CIT
100 nM CIT
Basal Respiration
Maximum Respiration
Relative oxygen consumption rate
siControl
siBMAL1

Figure S3

Figure S3. Insulin-regulated mitochondrial activity and BMAL1 are closely linked. Related to Figure 2. (A) Untreated and CIT cells were entrained by serum shock and cell lysate was collected every 4 h and assayed for NAD^+ and NADH levels (*left panel*). Untreated and CIT cells were assayed for steady state levels of NAD^+ and NADH (*right panel*). NAD^+ and NADH levels were normalized to cell number and the NAD^+/NADH ratio of untreated cells is set to 1. n=2. **(B)** Immunoblot analysis of protein from parental and ρ^0 MDA-MB-231 cells grown without insulin (Untreated) or chronic insulin treatment (CIT). **(C)** mRNA levels of *BMAL1* and its target gene *NAMPT* are shown from parental and ρ^0 cells either untreated or after CIT. Data are normalized to *GAPDH* and shown as mean±SEM; n=4. **(D)** Untreated and CIT MDA-MB-231 ρ^0 cells with deficient mitochondria were entrained by serum shock, and mRNA was collected every 4 h and subjected to qRT-PCR analyses. Transcript levels are normalized to constitutively-expressed *GAPDH* and mRNA of untreated cells at 0 h is set to 1. Data are shown n=4; $p>0.05$ at all time points. **(E-F)** Representative Mito Stress Test profile of CIT (10, 100 nM or not)-treated MDA-MB-231 cells. Mitochondrial oxygen consumption rate was measured before and after treatments with ATP synthase inhibitor oligomycin (O), mitochondria membrane uncoupler FCCP (F), and mitochondrial complex I inhibitor rotenone (R) in control- **(E)** or BMAL1-knockdown **(F)** MDA-MB-231 cells. **(G)** Basal respiration (*left panel*) and maximum respiration (*right panel*) calculated from **(E-F)**. **(A, C, G)** Data are shown as mean±SD; n=3; *: $p<0.05$; **: $p<0.01$; ***: $p<0.001$; independent samples t test.

Figure S3 Legend

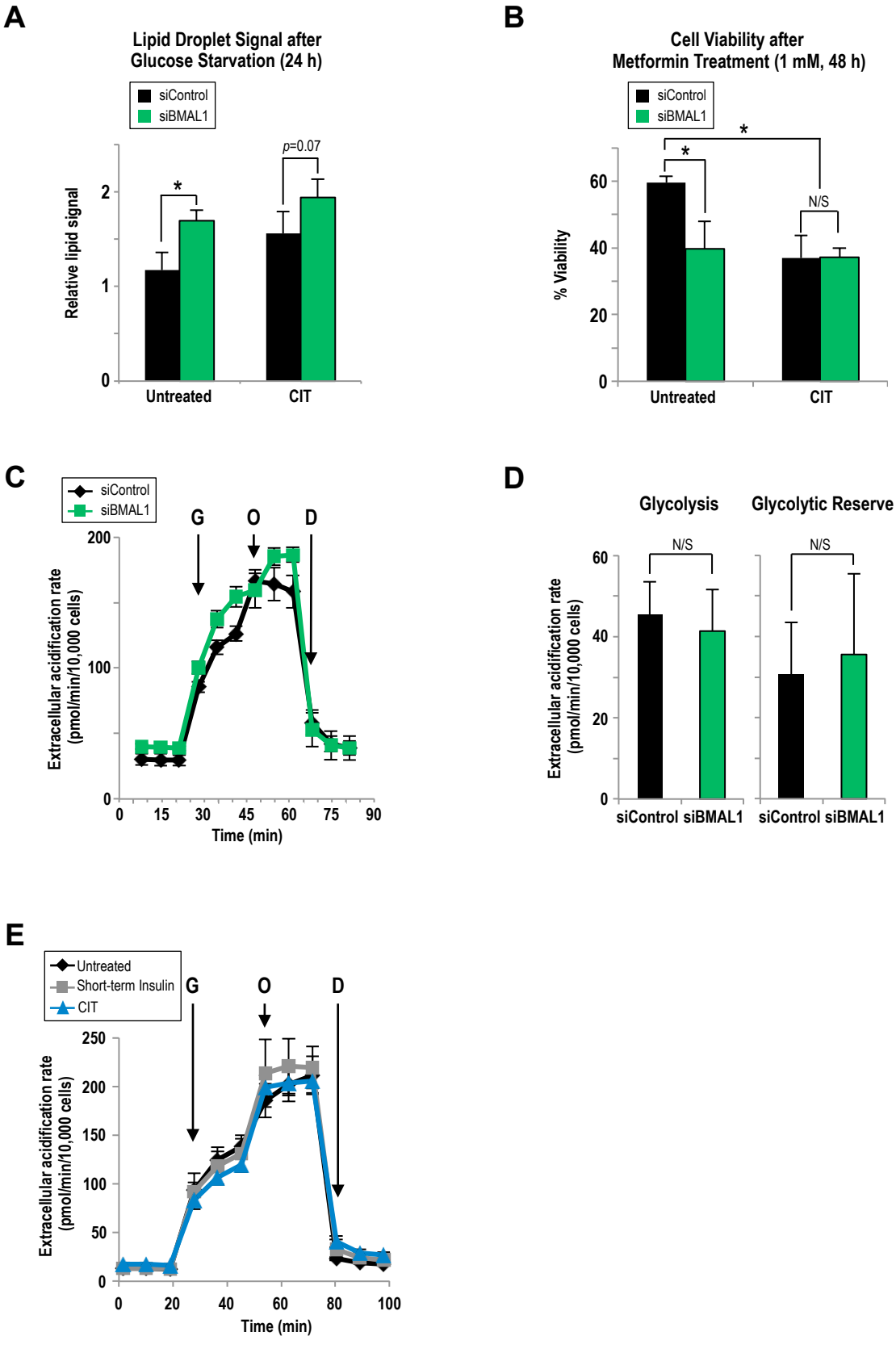
A
Lipid Droplet Signal after Glucose Starvation (24 h)
siControl
siBMAL1
Relative lipid signal
p=0.07
*
Untreated
CIT
B
Cell Viability after Metformin Treatment (1 mM, 48 h)
siControl
siBMAL1
% Viability
*
*
N/S
Untreated
CIT
C
siControl
siBMAL1
G
O
D
Extracellular acidification rate (pmol/min/10,000 cells)
Time (min)
D
Glycolysis
Glycolytic Reserve
N/S
N/S
Extracellular acidification rate (pmol/min/10,000 cells)
siControl siBMAL1
siControl siBMAL1
E
Untreated
Short-term Insulin
CIT
G
O
D
Extracellular acidification rate (pmol/min/10,000 cells)
Time (min)

Figure S4

Figure S4. BMAL1-mediated adaptation to CIT impacts glycolytic activity. Related to Figure 2. (A) MDA-MB-231 cells were grown without insulin (Untreated) or chronically treated with insulin (100 nM, CIT) and transiently transfected with control or BMAL1-targeting siRNA. Levels of neutral lipids were assayed after glucose starvation to assess ability to mobilize lipids during nutrient stress; n=3. **(B)** Cell viability was assayed after treatment with metformin (1 mM) in glucose-free media for 48 h. Data are shown as mean±SD; n=2. **(C)** One representative profile demonstrating Glycolysis Stress Test measuring ECAR before and after addition of glucose (G), ATP synthase inhibitor oligomycin (O), and glucose analog 2-deoxyglucose (D) in MDA-MB-231 cells were transiently transfected with BMAL1-targeting siRNA (or not) and seeded in glucose-free media. **(D)** Glycolysis and Glycolytic Reserve were calculated from panel C. Data are shown as mean±SD; n=2. **(E)** Glycolysis Stress Test profile is shown where ECAR was measured before and after glucose (G), oligomycin (O), and 2-deoxyglucose (D) treatment in MDA-MB-231 cells were grown without insulin (Untreated), with a 24 h pretreatment (Short-term) or over 10 passages with insulin (100 nM, CIT). ECAR is normalized to cell number. Data are shown as mean±SD; n=5; **(A, B, D)** N/S: $p>0.05$; *: $p<0.05$.

Figure S4 Legend

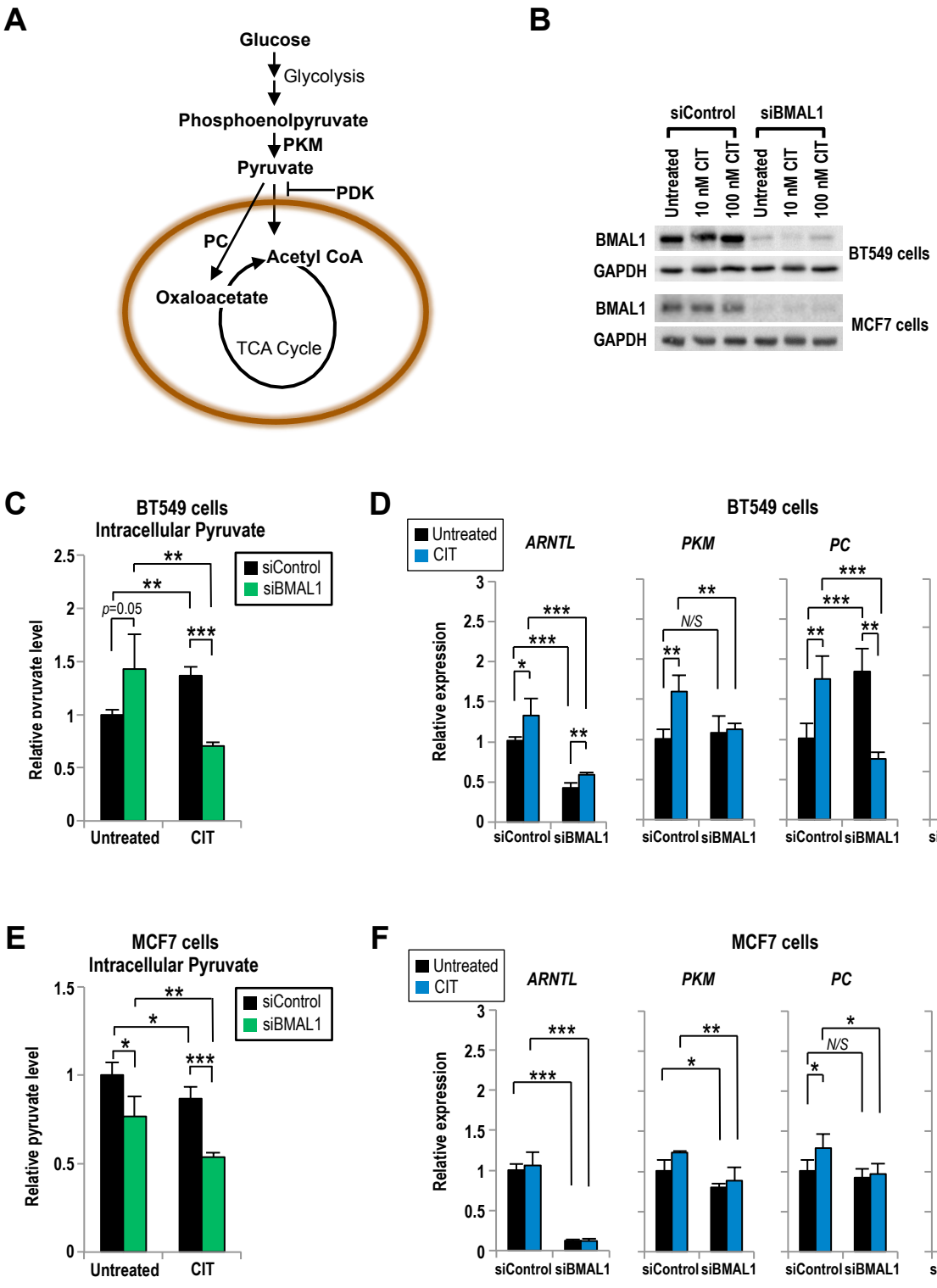
A
Glucose
Glycolysis
Phosphoenolpyruvate
PKM
Pyruvate
PDK
PC
Acetyl CoA
Oxaloacetate
TCA Cycle
B
siControl
siBMAL1
Untreated
10 nM CIT
100 nM CIT
Untreated
10 nM CIT
100 nM CIT
BMAL1
GAPDH
BT549 cells
BMAL1
GAPDH
MCF7 cells
C
BT549 cells
Intracellular Pyruvate
Relative pyruvate level
siControl
siBMAL1
p=0.05
Untreated
CIT
D
BT549 cells
Untreated
CIT
ARNTL
PKM
PC
PDK4
Relative expression
N/S
siControl
siBMAL1
E
MCF7 cells
Intracellular Pyruvate
Relative pyruvate level
siControl
siBMAL1
Untreated
CIT
F
MCF7 cells
Untreated
CIT
ARNTL
PKM
PC
PDK4
Relative expression
N/S
p=0.05
siControl
siBMAL1

Figure S5

Figure S5. BMAL1 affects pyruvate metabolism of cells adapted to CIT in BT549 and MCF7 cells. Related to Figure 2. (A) A general schematic diagram displaying the roles of the *PKM*, *PC*, and *PDK* enzymes in regulating intracellular pyruvate levels. **(B)** Immunoblots of BMAL1 in siControl- or siBMAL1-trasfected CIT (10 nM and 100 nM insulin) BT549 and MCF7 cells. **(C, E)** Relative intracellular pyruvate level in untreated and CIT (100 nM insulin) BT549 **(C)** and MCF7 **(E)** cells transfected with siControl or siBMAL1 for 16 h. Cells were treated with medium contain 10 mM glucose, no pyruvate, and 10% FBS for 48 h. **(D, F)** Relative mRNA level of pyruvate-regulating enzymes from untreated or CIT BT549 **(D)** and MCF7 **(F)** with or without BMAL1 knockdown by siRNAs, analyzed by qRT-PCR with *GAPDH* as loading control. **(C-F)** Data are shown as mean±SEM; n≥3; N/S: $p>0.05$; *: $p<0.05$; **: $p<0.01$; ***: $p<0.001$.

Figure S5 Legend

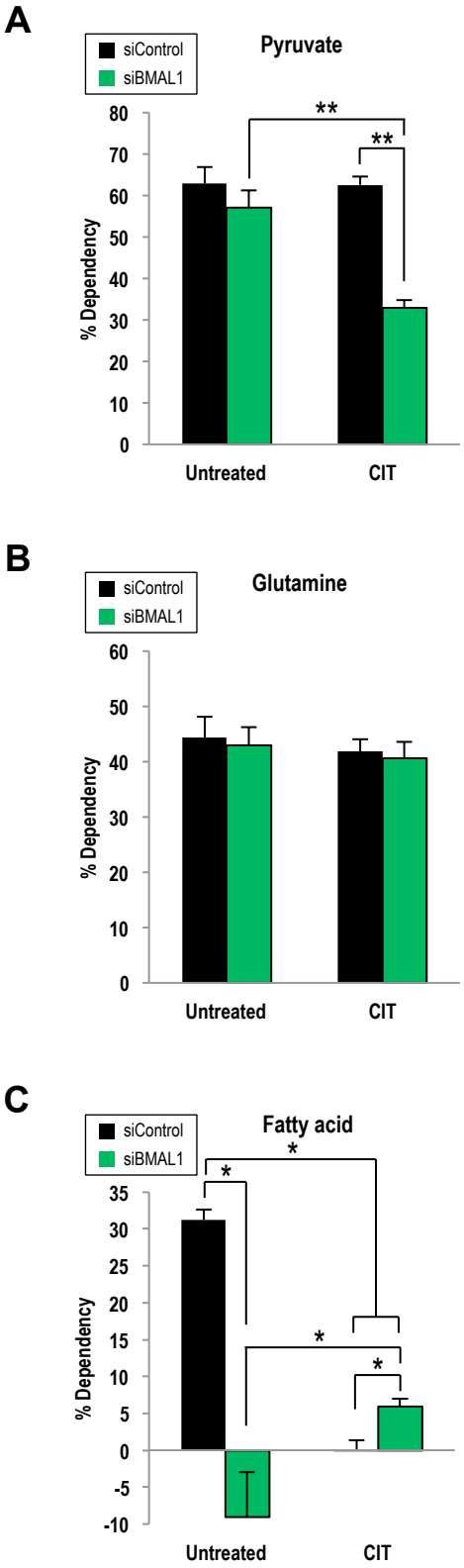
A
siControl
siBMAL1
Pyruvate
**
**
80
70
60
50
40
30
20
10
0
% Dependency
Untreated
CIT
B
siControl
siBMAL1
Glutamine
60
50
40
30
20
10
0
% Dependency
Untreated
CIT
C
siControl
siBMAL1
Fatty acid
*
*
*
*
35
30
25
20
15
10
5
0
-5
-10
% Dependency
Untreated
CIT

Figure S6

Figure S6. Influence of BMAL1 on mitochondria fuel dependency of chronic insulin treated cells. Related to Figure 2. (A-C) Control or siBMAL1-transfected MDA-MB-231 cells either without insulin treatment (Untreated) or CIT (100 nM insulin) were assayed for their respiratory dependence on pyruvate **(A)**, glutamine **(B)**, and fatty acids **(C)** in the Mito Fuel Flex Test. Data are shown as mean±SEM; n≥3; *: $p<0.05$; **: $p<0.01$.

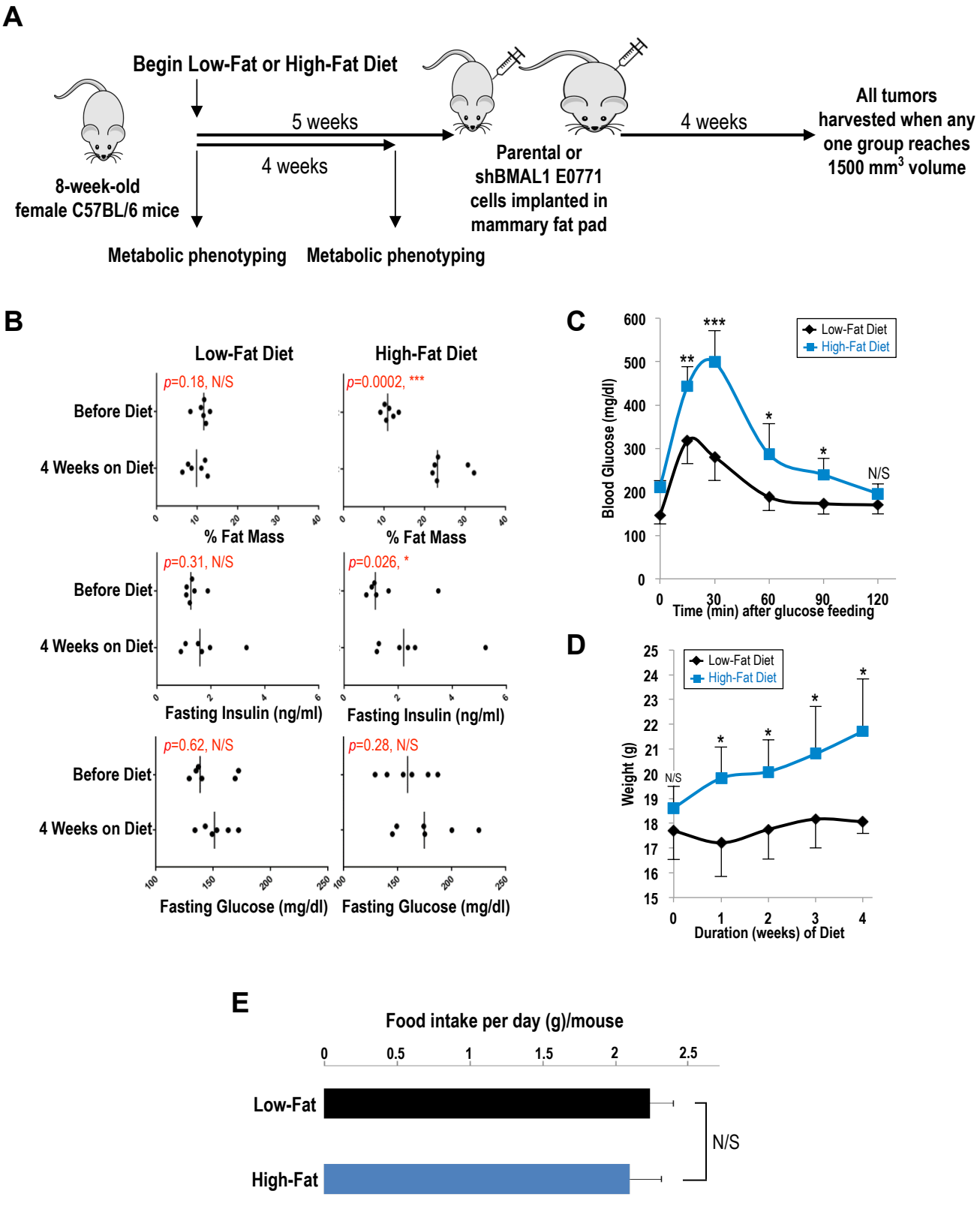
A
Begin Low-Fat or High-Fat Diet
5 weeks
4 weeks
4 weeks
All tumors harvested when any one group reaches 1500 mm3 volume
8-week-old female C57BL/6 mice
Parental or shBMAL1 E0771 cells implanted in mammary fat pad
Metabolic phenotyping
Metabolic phenotyping
B
Low-Fat Diet
High-Fat Diet
p=0.18, N/S
p=0.0002, ***
Before Diet
4 Weeks on Diet
% Fat Mass
p=0.31, N/S
p=0.026, *
Fasting Insulin (ng/ml)
p=0.62, N/S
p=0.28, N/S
Fasting Glucose (mg/dl)
C
Low-Fat Diet
High-Fat Diet
Blood Glucose (mg/dl)
Time (min) after glucose feeding
N/S
D
Weight (g)
Duration (weeks) of Diet
N/S
E
Food intake per day (g)/mouse
Low-Fat
High-Fat
N/S

Figure S7

Figure S7. HFD increases fat mass percentage and fasting insulin levels. Related to Figure 3. (A) Schematic diagram of animal experiment design. **(B)** Mouse body mass was measured by functional magnetic resonance imaging and fat mass percentage was calculated as fat mass divided by total mass (*upper panels*). Mice were fasted for five hours before serum was collected and assayed for insulin levels (*middle panels*) and glucose levels (*lower panels*). Measurements were taken before the controlled diet and after 4 weeks of low-fat diet (LFD) or high-fat diet (HFD). Data are shown as median values; n=6; paired samples t-test. **(C)** OGTT shows blood glucose levels measured in LFD- and HFD-fed mice at regular intervals 2 h after feeding; n=5. **(D)** Body weight of mice fed LFD or HFD was measured every week during the first four weeks of the diets; n=6. **(E)** Food intake per mouse was measured throughout the first four weeks of the LFD or HFD; n=6. **(C-E)** data are shown as mean±SD; N/S: $p>0.05$; *: $p<0.05$; **: $p<0.01$; ***: $p<0.001$; independent samples *t* test.

Figure S7 Legend

Transparent Methods

Cell Culture

Human cell line MDA-MB-231 (Cat No. HTB-26) was purchased from American Type Culture Collection (ATCC, Manassas, VA, USA). MDA-MB-231 cells were grown in Dulbecco's modified Eagle's medium (DMEM) with high glucose (25 mM), L-glutamine (4 mM), and sodium pyruvate (1 mM) (Corning, 10-013) at 37°C, 5% CO_2 in a humidified chamber. All media were supplemented with heat-inactivated fetal bovine serum (10%, v/v) (Thermo Fisher, 10437028) and 1X antibiotics containing penicillin and streptomycin (Corning, 30-002-CI). No. 25-512, Genesee). MDA-MB-231 ρ^0 were cultured in the same media as the MDA-MB-231 cells with a supplement of uridine (50 µg/ml) and ethidium bromide (50 ng/ml). The cells were grown in incubators set at 37 ºC at 5% CO_2. All cells used in this study were tested and found to be mycoplasma negative. Prior to insulin treatment, MDA-MB-231 cells were serum depleted in DMEM high glucose (25 mM) medium containing BSA (0.2%, serum-free medium) for 24 h and then stimulated with Insulin (100 nM, Cat No. I9278; Sigma-Aldrich, St. Louis, MO) or left untreated for indicated time periods. For metformin treatment and cell viability assay, cells were seeded in equal numbers in plates with glucose-free media containing metformin (0 or 1 mM, Sigma, PHR1054) and incubated at 37 ºC with CO_2 for 48 h. Cells were counted using a hemocytometer and trypan blue dye as well as with the Cytation 5 Imaging Reader (Biotek). Viability was calculated as a percentage of live cells in metformin-treated wells compared to live cells in wells without metformin.

Parental E0771 cells were obtained from CH3 BioSystems (Cat No. 940001). Parental and stably transduced E0771 shBMAL1 cells were grown in RPMI 1640 media with glutamine (2.05 mM; GE Life Sciences, SH30027) and supplemented with fetal bovine serum (5%) and HEPES (10 mM). DNA encoding shRNA targeting mouse *Arntl* in a pLKO.1 lentiviral backbone was obtained the Broad Institute RNAi Consortium. pΔ8.7 and pVSV-G were transfected with the pLKO.1 plasmid using Lipofectamine 2000 reagent (Thermo Fisher, 11668) into HEK 293T cells to generate lentivirus. To transduce E0771 cells with lentivirus, the cells were grown in virus-infected media with polybrene (2 µg/ml). Successfully transduced cells were selected by puromycin as described previously (Cheng et al., 2016).

Short-term insulin treated cells were first starved with serum-free DMEM for 24 h and incubated with insulin (100 nM)-containing medium for 24 h. To establish cells subjected to chronic insulin treatment (CIT), cells were cultured in growth medium containing human recombinant insulin (100 nM; Thermo Fisher, 12585014) for at least 10 passages. For cell entrainment, cells were grown overnight in serum-free media, then incubated in DMEM with fetal bovine serum (50%)

for 2 h using a previously described serum shock procedure (Balsalobre et al., 1998). The entrained cells were washed with phosphate buffered saline after the serum shock and were grown in serum-free media for the remainder of the experiments.

For culturing cells from excised tumor, tumor mass was minced and digested with 1X collagenase/hyaluronidase (Stem Cell Technologies, 07912) at 37 ºC for 1 h, with pipetting through a 10-ml serological pipet every 15 min. Cell suspension was passed through a 70-µm strainer and red blood cells were lysed with ACK Lysing Buffer (Thermo Fisher, A1049201) for 1 min. After centrifugation, cells in supernatant were cultured in media for E0771 cells.

Western Blot

Cells were seeded at a density of 5×10^5 cells per well in six well plates. The medium was changed to serum-free medium at 48 h post-seeding. Insulin (100 nM in serum-free medium) was added at 24 h following serum/insulin removal for indicated time periods. Cells were collected by scraping and centrifugation at 800×g for 5 mins at 4°C. Cell pellet was washed once with PBS and resuspended in 20 cell volumes of 1X SDS sample buffer. Cell lysates were prepared by performing two iterations of vortexing and heating at 95°C for 5 mins. Western blotting was performed by running cell lysates on a gradient SDS-PAGE gel and transferring onto a PVDF membrane. Western blots were probed with antibodies specific to BMAL1, GAPDH (Santa Cruz, sc-365645 and sc-25778, respectively), p-Akt-S473, Akt, p-Insulin Receptor-Y1150/1151, Insulin Receptor β, tubulin (Cell Signaling Technology, 9271, 9272, 3024, 3025 and 2125S, respectively), NAMPT (Novus, 2361), Actin (Millipore, MAB1501R), and MitoProfile OXPHOS Cocktail (Abcam, ab110411). Images were obtained and analyzed using ChemiDoc Touch Imaging System and Image Lab software (Bio-Rad). After primary antibody incubation, blots were incubated with HRP-conjugated anti-rabbit or anti-mouse secondary antibodies (1:5000 dilution; Abcam, ab6721 and ab6789) and protein bands were visualized using chemiluminescence detection. The intensity of desired non-saturated protein bands was quantified and normalized to Actin.

ATP measurement

For ATP measurement, MDA-MB-231 cells untreated or treated with insulin in 12-well plates. Cells were lysed in 1% trichloroacetic acid and 0.1% tris-acetate. The lysate was clarified by centrifugation at 16000×g for 10 mins at 4°C. ATP levels were measured using the luciferase-based ENLITEN ATP Assay System (Promega, FF2000) and detected using the Synergy H1 Microplate Reader (Biotek). Measurements were normalized to cell number.

Quantitative RT-PCR analysis

RNAs were isolated by homogenizing cells with QIAshredder columns (QIAGEN, 79654) and purifying RNA using the Quick-RNA Kit (Zymo, R1054). cDNA was synthesized using the iScript Kit (Bio-Rad, 1708890) and the qRT-PCR reaction utilized the components contained in the iTaq Universal SYBR Green Supermix (Bio-Rad, 1725120). Reaction was performed in the iQ5 Thermal Cycler (Bio-Rad) and data was analyzed by the $2^{\Delta\Delta Ct}$ method and normalized to *GAPDH*. The sequences of primer pairs used are:

ARNTL (5'-GCTCAGGAGAACCCAGGTTATC and 5'-GCATCTGCTTCCAAGAGGCTCA),
GAPDH (5'-CCCCTTCATTGACCTCAACTA and 5'-CTCCTGGAAGATGGTGATGG),
NAMPT (5'-CCAGAGCTCCCAGACTGC and 5'-GTGGCCAGGAGGATGTTGAA),
PKM (5'-ATGGCTGACACATTCCTGGAGC and 5'-CCTTCAACGTCTCCACTGATCG),
PC (5'-GCCATGTCATGGTAAACGGTCC and 5'-GCAGGATGTCTCTGAAACCAGC),
PDK2 (5'-TGCCTACGACATGGCTAAGCTC and 5'-GACGTAGACCATGTGAATCGGC).

NADH and NAD^+/NADH analysis

Samples were prepared using reagents from the NAD/NADH-Glo Assay Kit (Promega, 9071). Briefly, the siRNA-transfected MDA-MB-231 cells were seeded in 96-well white opaque plates, and sets of cells underwent serum shock every 4 h so that all time points of NAD^+ and NADH samples were harvested at the same time. Cells were lysed using solution containing Trizma base, hydrochloric acid, and dodecyltrimethylammonium bromide per the instructions in assay kit. Luminescence was detected using the Synergy H1 Microplate Reader (Biotek).

Genetic knockdown by siRNAs

The siRNAs are pooled sets of three target-specific siRNAs that are 19 to 25 nucleotides long. siRNAs were used to knock down expression of BMAL1/*ARNTL* and PKM (Santa Cruz, sc-38165 and sc-62820, respectively). The control siRNA (Santa Cruz, sc-37007) contains a scrambled sequence and served as a negative control. The transfection reaction used Lipofectamine RNAiMAX (Thermo Fisher, 13778150) and the manufacturer-recommended protocol using Opti-MEM I Reduced Serum Medium (Thermo Fisher, 11058021).

Mito Stress Test assay

One day prior to assay, cells were counted and seeded $5x10^4$ on assay plate in XF Assay Medium (Agilent, 102365) supplemented with glucose (25 mM) and pyruvate (1 mM) overnight. During assay, cells were sequentially injected to obtain final concentrations of oligomycin (1 μM), trifluoromethoxy carbonylcyanide phenylhydrazone (0.5 μM, FCCP), and rotenone (2.5 μM) according to manufacturer's protocol. Oxygen consumption rate (OCR) was measured using the

Seahorse Extracellular XFe96 Analyzer (Agilent) and normalized to cell number. Basal respiration is calculated as the OCR measurement prior to oligomycin injection subtracted by the measurement after rotenone injection. Maximum respiration is the OCR measurement after FCCP injection subtracted by the measurement after rotenone injection.

Glycolysis Stress Test assay

Cells were seeded as in OCR assays. During the assay, cells were sequentially injected to obtain final concentrations of glucose (10 mM), oligomycin (1 μM), and 2-deoxyglucose (50 mM) according to manufacturer's protocol. Extracellular acidification rate was measured using the Seahorse Extracellular XFe96 Analyzer (Agilent) and normalized to cell number. Glycolysis is calculated as the ECAR measurement after glucose injection subtracted by the measurement before glucose injection. Glycolytic reserve is the ECAR measurement after oligomycin injection subtracted by the measurement after glucose injection.

Neutral lipid assay

Cells were harvested by trypsinization, and incubated for 30 mins in the dark with BODIPY 493/503 (5 ng/ml, Thermo Fisher, D3922) solution for dyeing neutral lipids. Fluorescent-labeled lipids were detected using BD Accuri C6 Cytometer. Results are reported as relative fluorescence.

Pyruvate assay

Cells were harvested by scraping and lysed with reagents from Pyruvate Assay Kit (Abcam, ab65342). The probe and enzyme from the kit catalyzed a fluorescent with the pyruvate in the sample, and fluorescence was detected at 535/587 nm using the Synergy H1 Microplate Reader (Biotek). Measurements were normalized to cell number.

Mitochondrial ROS assay

Cells were incubated with MitoSOX (3 μM, Thermo Fisher, M36008) for 10 mins at 37 ºC to stain mitochondria-specific superoxide. After staining, the cells were fixed with 2% paraformaldehyde on ice. Fluorescent-labeled mitochondrial superoxide was detected using BD Accuri C6 Cytometer.

Viability assay

To assess viability of cells, cells were stained with trypan blue dye and counted using a hemocytometer. Dead cells were identified as those whose membranes were permeated by the blue dye. Viability is indicated as the percentage of live cells out of total cells.

Mito Fuel Flex Test assay

Substrate utilization in cells was measured using the Seahorse XF Mito Fuel Flex Test Kit (Agilent Technologies, 103260) as previously described. On day of assay the cells were seeded in XF Base Medium (Agilent, 102353) supplemented with glucose (25 mM), sodium pyruvate (1 mM), and L-glutamine (2 mM). For this assay, BPTES (4 μM), Etomoxir (10 μM) or UK5099 (5 μM) were used to inhibit glutamine, FA or glucose oxidation. OCR was measured using the Seahorse Extracellular XFe96 Analyzer (Agilent). To calculate fuel dependence percentage, or the cell's reliance on a particular fuel pathway, this equation was used: (basal OCR – OCR after treatment with target inhibitor)/(basal OCR – OCR after treatment with all fuel inhibitors). To calculate fuel capacity percentage, or the cell's ability to oxidize a fuel when other pathways are inhibited, this equation was used: 1 – [(basal OCR – OCR after treatment with other two inhibitors)/(basal OCR – OCR after treatment with all fuel inhibitors)]. Fuel flexibility was calculated as the absolute value of the difference between capacity and dependence.

Gene expression profile analysis

Gene expression data from the TCGA Pan-Cancer project (Cancer Genome Atlas Research Network et al., 2013) was applied to this study. Log2-transformed RNA-Seq by Expectation-Maximization (RSEM) expression values were used for boxplots, clustering analysis and GSEA. Morpheus software by Broad Institute (https://software.broadinstitute.org/morpheus/) was used for heatmap generation and unsupervised hierarchical clustering analysis with one minus Pearson correlation distance. GSEA (http://software.broadinstitute.org/gsea) was performed based on a ranked gene list derived from the correlation of expression between *ARNTL* and genes from Gene Ontology biological process gene sets (Molecular Signatures Database v6.2). The RNA-Seq data from BC cell lines was obtained from Heiser *et al* (Heiser et al., 2012) and unpublished observations kindly provided by Joe Gray (Oregon Health & Science University). Kaplan-Meier curves representing the distal metastasis-free of patient groups were plotted according to the expression of the BMAL1. Log-rank statistics were applied to identify the optimal cut-point for transforming the continuous variable of BMAL1 gene expression into categorical high and low expression groups in a survfit model. Each curve represents the percentage (Y-axis) of the population that exhibits distal metastasis along time (X-axis, in months). Vertical ticks indicate censored patients. A Log-rank test is performed to compare the differences in the two groups.

Animals

Animal experiments were approved by the Institutional Animal Care and Use Committee at City of Hope (IACUC 10024). Female C57BL/6-Tg(UBC-GFP)30Scha/J mice were obtained from Jackson Laboratory. The 8-week-old mice were divided into four groups with at least six animals in each group. Two groups were fed with high-fat diet (HFD, 60% of total calories as dietary fat; Research Diets, D12492) or low-fat, sucrose-matched diet (LFD, 10% of total calories as dietary fat; Research Diets D12450J) for five weeks. Both HFD- and LFD-fed of mice were then randomly separated into two equal groups and each group was injected with E0771 parental or shBMAL1 cells ($2x10^5$) at the right 4^{th} mammary fat pad and fed with same diet until euthanization. Tumor size, mouse body weight, and food intake were measured twice per week. Tumor size was calculated with the equation $(length \times width^2)/2$. Tumor masses and lung tissue were excised *en bloc*. Part of tumor mass was fixed in neutral-buffered formalin (10%) for at least three days. Tissue embedding, sectioning, and Ki67 immunohistochemistry staining were performed by the City of Hope Molecular Pathology Core. Lung tissue was fixed in formalin for at least three days before counting nodules.

Metabolic phenotyping

Body composition analysis, oral glucose tolerance test, fasting insulin, and fasting glucose measurements were performed by the City of Hope Comprehensive Metabolic Phenotyping Core. Fat mass and weight were measured with an EchoMRI a body composition analyzer. For oral glucose tolerance test, mice were fasted for five hours, orally fed glucose and tail vein blood drawn every hour to measure glucose levels. For fasting blood glucose, mice were fasted for five hours and tail vein blood was drawn to measure glucose levels. For fasting insulin, mice were fasted for five hours and tail vein blood was drawn to measure insulin in an enzyme-linked immunosorbent assay.

Statistical analyses

Data are represented as mean and standard error of mean (Mean ± SEM). Statistical analyses were performed using GraphPad Prism 7.0 software (GraphPad Prism Software Inc., San Diego, CA) and R. Normal distribution was confirmed using Shapiro-Wilk normality test before performing statistical analyses. For normally distributed data, comparison between two means were assessed by unpaired two-tailed Student's t test and that between three or more groups were evaluated using one-way analysis of variance (ANOVA) followed by Tukey's post hoc test. In animal studies, paired t test was performed to analyze metabolic measurements of individuals before and after HFD or LFD feeding regimen. Brown-Forsythe test confirmed that the variance

in the groups compared were not significantly different. All data followed a normal distribution and have equal variances. A *p*-value lower than 0.05 was considered statistically significant. Figures were generated using Adobe Illustrator software (San Jose, CA, USA). Power analysis was performed by Power and Sample Size Calculations program (Dupont and Plummer, 1990). In each of the independent sample groups containing at least six mice, there is about a 25% standard deviation between tumor sizes. An effect size of 0.5 between groups with this sample size will detected with over 87% power.

Supplemental References

Balsalobre, A., Damiola, F., and Schibler, U. (1998). A serum shock induces circadian gene expression in mammalian tissue culture cells. Cell *93*, 929-937.

Cancer Genome Atlas Research Network, Weinstein, J.N., Collisson, E.A., Mills, G.B., Shaw, K.R., Ozenberger, B.A., Ellrott, K., Shmulevich, I., Sander, C., and Stuart, J.M. (2013). The Cancer Genome Atlas Pan-Cancer analysis project. Nat. Genet. *45*, 1113-1120.

Cheng, C.T., Kuo, C.Y., Ouyang, C., Li, C.F., Chung, Y., Chan, D.C., Kung, H.J., and Ann, D.K. (2016). Metabolic stress-induced phosphorylation of KAP1 Ser473 blocks mitochondrial fusion in breast cancer cells. Cancer Res. *76*, 5006-5018.

Dupont, W.D., and Plummer, W.D., Jr. (1990). Power and sample size calculations. A review and computer program. Control. Clin. Trials *11*, 116-128.

Heiser, L.M., Sadanandam, A., Kuo, W.L., Benz, S.C., Goldstein, T.C., Ng, S., Gibb, W.J., Wang, N.J., Ziyad, S., Tong, F., et al. (2012). Subtype and pathway specific responses to anticancer compounds in breast cancer. Proc. Natl. Acad. Sci. U.S.A. *109*, 2724-2729.